Version of Record: https://www.sciencedirect.com/science/article/pii/S0928493118307707
Manuscript_d00578970e3a8dee6003336dead0674f

Synthesis of calcium-deficient hydroxyapatite nanowires and nanotubes performed by template-assisted electrodeposition

Sylvie Beaufils [a,b,1*], Thierry Rouillon [b], Pierre Millet [a,1,2], Jean Le Bideau [c], Pierre Weiss [b,3,4], Jean-Paul Chopart [a,1], Anne-Lise Daltin [a,1]

[a] LISM, URCA, B.P. 1039, 51687 Reims Cedex 2, France

[b] Inserm, UMR 1229, RMeS, Regenerative Medicine and Skeleton, Université de Nantes, ONIRIS, Nantes, F-44042, France

[c] Institut des Matériaux Jean Rouxel (IMN), Université de Nantes, CNRS, 2 rue de la Houssinière, BP 32229, 44322 Nantes cedex 3, France

[1] Université de Reims-Champagne Ardennes, UFR Odontologie, Reims 51100, France

[2] CHU Pôle de Médecine Bucco-Dentaire, Reims 51100, France

[3] Université de Nantes, UFR Odontologie, Nantes, F-44042, France

[4] CHU Nantes, PHU4 OTONN, Nantes, F-44093, France

* corresponding author: Tel./fax (33)3 26 91 84 49 ; e-mail addresses : **sylvie.beaufils@univ-nantes.fr**

Abstract:

Hydroxyapatite (HA) has received much interest for being used as bone substitutes because of its similarity with bioapatites. In form of nanowires or nanotubes, HA would offer more advantages such as better biological and mechanical properties than conventional particles (spherical). To date, no study had allowed the isolated nanowires production with simultaneously well-controlled morphology and size, narrow size distribution and high aspect ratio (length on diameter ratio). So, it is impossible to determine exactly the real impact of particles' size and aspect ratio on healing responses of bone substitutes and characteristics of these ones ; their biological and mechanical effects can never be reproducible. By the template-assisted pulsed electrodeposition method, we have for the first time succeeded to obtain such calcium-deficient hydroxyapatite (CDHA) particles in aqueous baths with hydrogen peroxide by both applying pulsed current density and pulsed potential in cathodic electrodeposition. After determining the best conditions for CDHA synthesis on gold substrate in thin films by X-

© 2018 published by Elsevier. This manuscript is made available under the CC BY NC user license
https://creativecommons.org/licenses/by-nc/4.0/

Ray diffraction (XRD) and Energy dispersive X-Ray spectroscopy (EDX), we have transferred those conditions to the nanowires and nanotubes synthesis with high aspect ratio going until 71 and 25 respectively. Polycrystalline CDHA nanowires and nanotubes were characterized by Scanning electron microscopy (SEM) and Transmission electron microscopy (TEM). At the same time, this study enabled to understand the mechanism of nanopores filling in gold covered polycarbonate membrane: here a preferential nucleation on gold in membranes with 100 and 200 nm nanopores diameters forming nanowires whereas a preferential and randomly nucleation on nanopores walls in membranes with 400 nm nanopores diameter forming nanotubes.

Keywords: electrodeposition, calcium deficient hydroxyapatite, nanowires, nanotubes, template synthesis

1. Introduction

Hydroxyapatite ($Ca_{10}(PO_4)_6(OH)_2$, HA), with a Ca/P ratio of 1.67, has attracted much attention because of its chemical and structural similarities with the key mineral component of human bone and teeth. HA is the thermodynamically most stable [1], the densest and the less soluble calcium phosphate (CaP). Due to its excellent biocompatibility, bioactivity, osteoconductivity and high compressive strength, HA and derivated are largely used in orthopaedic, dental and maxillofacial applications such as bone substitutes. But bone is constituted of nanocrystalline, non-stoichiometric, calcium-deficient apatites generally described by the following formula $Ca_{10-x}(PO_4)_{6-x}(HPO_4)_x(OH)_{2-x}$, [2] whose Ca/P molar ratio can go from 1.33 up to 1.67 [3]. Because of a lower Ca/P ratio than HA, calcium-deficient hydroxyapatite (CDHA) benefits from a higher solubility and consequently it biologically appears more bioactive than HA [4, 5]. So CDHA, whose composition and structure are very close to the natural bone mineral, is

of greater biological interest [6] than stoichiometric HA and a suitable candidate for bone regeneration [7].

Biological and mechanical properties of calcium phosphates are affected by the size, morphology, composition and structure of the particles. CaP nanoceramics, whose progresses in nanotechnology have allowed their fabrication since 1994 [8], are hopeful of becoming a new generation of bone substitutes. The scientific efforts made in development of novel CaP formulations should lead to improved biomaterials, more suitable and effective for various biomedical applications. CaP materials can be used to reinforce polymer matrices and bone cements, porous 3D scaffolds for bone tissue engineering or for drug delivery. Because of their restricted size, high specific surface area, multiadsorbing sites and more favorable surface topography, nanoparticles [9] and particularly one-dimensional (1D) nanostructures such as nanorods, nanotubes [10], nanowires and nanowhiskers [11] have recently attracted much interest owing to their unique and remarkable properties (high aspect ratio, preferable biocompatibility, higher solubility, enhanced biological [9, 12, 13, 14] and mechanical properties [15, 16] …) and their potential use in many applications. Nanoparticles [9, 12] and nanophase ceramics [18] can selectively and easier adsorb more specific proteins, enhance the adhesion and proliferation of osteoblasts, increase osteoblastic functions resulting in higher osteoconductivity and bioactivity than conventional particles and microphases ceramics. The integration of CaP nanowires [19] or nanotubes [17] is expected to enhance composites' properties and mechanical strengthening. Therefore, such materials are excellent candidates for scaffolds in bone tissue engineering and bone substitutes [20].

HA nanofibers, nanowires or nanotubes have been produced by different methods such as

hydrothermal process (the most useful method) [21], solvothermal process [22], or hydrothermal and sol-gel associated methods [23], nevertheless the majority of these methods enabled to obtain HA nanowires with a too wide size distribution [23, 24, 25], irregular and non-controlled morphology with an average aspect ratio (length on diameter ratio) limited to 30-50 [26, 27, 28]. This introduces major disadvantages: it is impossible to determine exactly the real impact of particle's size and aspect ratio on healing responses of composite bone substitutes and their inconstant parameters forbid any reproducibility of the results. To date, no study had allowed the isolated nanowires production with well-controlled morphology and size and high aspect ratio by the template-assisted electrodeposition method.

The template method could be the only way to produce particles whose structure, morphology, size and array are well controlled. The use of the template method, for assisting metallic wires synthesis, was related by Bean in 1969 for the first time [29], followed by Possin by means of a porous etched mica and electroplating method [30]. Masuda and Fukuda were the first to report, in 1995, an ordered pores arrangement in anodic aluminium oxide membrane [31]. Then researchers used track-etched polycarbonate membranes [32].

Our study is the first that presents the synthesis of CDHA nanowires and nanotubes by using a template-assisted electrodeposition, with the exception of a study from Wang *et al.* who realized a highly ordered HA nanowires array (about 200 nm in diameter and 1µm in length) and low aspect ratio of 5 [32]. Our method based on a pulsed electrodeposition with a recovering of nanowires separately should enable us to achieve much higher aspect ratios. Electrochemical deposition (ECD): one of the most common methods, offers many advantages such as low processing temperatures, a fast growth rate, a uniform deposition on irregular shapes and low

cost. The quality of the deposits can be optimized by controlling the deposition parameters [33]. Recent studies have shown that coatings obtained by pulsed electrodeposition in presence of hydrogen peroxide (H_2O_2) showed less holes and craters, more uniformity, better adhesion and better mechanical properties than coatings produced with a constant potential [34]. It was also described that pulsed deposition allowed the growth of smaller crystallites than continuous deposition usually did and we hypothesized that it favored nanowires formation.

The final objective of this work was to synthesize HA nanowires (or nanotubes) of very high aspect ratios with a regular and controlled morphology while offering a selection of 1D nanostructures with different diameters for several applications. In order to define the best parameters of the electrodeposition, we started by testing the electrodeposition in thin films on gold covered disks, using many deposition parameters and analysing the results. Our hypothesis is that the best parameters used in thin layers deposits should be similar to those we should use for the template method.

The present work presents the analysis by X-Ray diffraction of these powders obtained from thin films crushing before and after a heat treatment at 850°C, which enabled us to certify the exclusive presence of CDHA as crystalline phase. Finally, the optimized parameters for HA electrodeposition were transposed to the template method for elaborating high aspect ratio nanowires and nanotubes. Their characterizations were undergone by Scanning electron microscopy and Transmission electron microscopy.

2. Materials and methods

2.1. Electrolyte preparation

The aqueous electrolyte bath was similar to the first one proposed by Shirkhanzadeh *et al.* in 1994; 0.042 mol.L^{-1} of $Ca(NO_3)_2$ and 0.025 mol.L^{-1} of $NH_4(H_2PO_4)$ were dissolved at room temperature in deionised water with a Ca/P ratio of 1.67 corresponding to the stoichiometric HA [8]. 0, 6 and 9 vol.% H_2O_2 were added in the bath in order to prevent hydrogen bubbles formation during electrodeposition and to favour a better calcium phosphate crystals nucleation [34, 35]. H_2O_2 makes able to obtain different calcium phosphates; its concentration modifies the pH value of the bath. This one was adjusted to 4.5 or 6.0 by adding NaOH [33, 36]. A forced convection was applied by using a peristaltic pump, in order to prevent settling, for keeping a stable composition of the bath around the cathode and for pumping hydrogen bubbles that can get into nanopores and alter the composition and structure of the synthesized material. Bath stirring was also reported helpful for obtaining CaP crystals in nanosize [37].

2.2. Electrodes preparation

Experiments were performed in a three-electrode cell. Pt wire acts as the auxiliary electrode; before using, it was cleaned with 99.9° alcohol then heated in a hydrogen flame till red glow. An Ag/AgCl electrode was used as the reference electrode. The working electrodes were firstly stainless steel disks, then once the electrodeposition parameters selected, track-etched polycarbonate membranes were used as cathodes. The disks were mechanically polished with increasingly finer grades of SiC paper, rinsed with alcohol 99,9° and dried. Then, they were covered with a 300 nm gold film by a physical vapor deposition process. The gold covered disks active surface area for the deposits was 0.125 cm². For the nanowires synthesis, Whateman® Cyclopore nuclear track-etched polycarbonate membranes were used as a template. Three references of membranes have been used (100, 200 and 400 nm pore diameters) with 11 µm nominal thickness. One side of the membrane was coated by sputtering with a 300 nm

gold film. This conductive film acts as the cathode. The pores densities quoted by the supplier and the active surface area (total area of the pores) were respectively 6.10^8/cm² and $5.89.10^{-3}$ cm² for membranes with pores of 100 nm diameter, 5.10^8/cm² and $1.96.10^{-2}$ cm² for membranes with pores of 200 nm diameter and $1.5.10^8$/cm² and $2.38.10^{-2}$ cm² for membranes with 400 nm pores diameter. The horizontal upward working electrode was connected to the potentiostat.

2.3. Experimental setup

The cathodic electrodeposition was conducted in an electrochemical cell made of glass with a polymer covering (Fig. 1a)). The three electrodes were immerged in an electrolytic bath whose temperature was maintained at 70°C using a hot water flow in a double-wall electrochemical cell [38]. In the sample holder made of polymer, the stainless steel disks and membrane disks were maintained between a join and a screw. A stainless steel grid was interposed between the cathode and the disks. The distance between counter and cathodic electrodes was fixed at 20 mm. The reference electrode (Ag/AgCl) was maintained in proximity to the cathode.

2.4. Electrodeposition

The cathodic depositions were carried out under a vertical laminar flow hood with a Radiometer PGZ301 Potentiostats controlled by VoltaMaster4 software operating in static and pulsed mode. Before deposition, the membranes were placed into the electrolytic bath for 4 minutes so as to impregnate them with it.

Preliminary cyclic voltammetry (CV) experiments were carried out on a gold covered stainless steel disk at 70°C and conducted at a scan rate of 10 mV/s (Fig. 2). The electrodeposition was performed at 70°C in a potentiostatic or intentiostatic mode. The effective period of deposition was 3 minutes, 5 minutes [39], 10 minutes and 15 minutes. The final chosen value of effective potential was -1.6 $V/_{Ag/AgCl}$ according to other studies [8]. The values of current density applied for thin films in constant mode (-15 and -20 $mA.cm^{-2}$) were chosen in accordance with works which succeeded to electrodeposit HA [34, 39, 40]. Deposition in membrane was successful only for higher values of current density [40, 41, 42], so an effective value of -120/ -250 $mA.cm^{-2}$ was applied correspondingly to the average values registered during a potential imposition of -1.6$V/_{Ag/AgCl}$ [43]. Electrodeposition was firstly carried out in constant mode and then in pulsed mode (Fig. 1.b). The conditions of pulsed electrodeposition were those chosen by Drevet *et al.* [34]; five deposition cycles were imposed, each one was composed by a deposition time (60 s; E = -1.6 $V/_{Ag/AgCl}$ or I = -120 or -150 $mA.cm^{-2}$), followed by a break time (120 s; value of free potential or 0 $mA.cm^{-2}$ respectively). Some deposits were realized by alternating 1s deposition time and 2s break time such as metallic nanowires produced in others studies [44]. A low frequency pulse was chosen to give the system time to recover during the off period. Chrono-potentiometric and chrono-amperometric curves were followed (Fig. 1b).

Table 1 presents the varied electrodeposition parameters tested to obtain the different thin films on gold covered stainless steel disks. Samples a, b, c and d were obtained in a constant mode with a potential of -1.6V $/_{Ag/AgCl}$ respectively applied with 0, 6 and 9 % vol. H_2O_2 at pH 6.0 and 4.8. The onset current density could vary between -1 and -110 $mA.cm^{-2}$. The other samples were deposited with 9% vol. H_2O_2, at pH 4.5 (e, f) and pH 6.0 (g, h), in a constant (e, g) and pulsed mode (f, h) (t_{ON} = 1 min and t_{OFF} = 2 min) by applying a potential of -1.6 V $/_{Ag/AgCl}$.

2.5. Thin films and nanowires / nanotubes characterization

Thin films obtained were characterized by a Bruker Analytical D8 Advance X-Ray diffractometer operating with a Cu Kα radiation (λ = 1.5418 Å) at 40 kV and 40 mA, in the θ-θ mode. X-Ray patterns data (Fig. 3' and 3") were collected in the 2θ range between 3 and 70°, with a 2θ step of 0.04°, a counting time of 2 seconds by step and a 30 rpm for spinning speed of the sample holder. The chemical composition of thin films (Ca/P molar ratios) was investigated by energy dispersive X-ray spectroscopy (EDX). SEM analysis was performed using a JSM-6460LA microscope (Jeol) operating at 13 kV and results of the Ca/P atomic ratio were reported as the mean of measurements.

In order to differentiate HA and OCP, a heat treatment of the calcium phosphate powders obtained by thin films crushing have been done such as Karampas *et al.* works [45]. The deposits were subjected to a temperature of 850°C under N_2 flow, during 2 hours after an increasing and before a decreasing in temperature of 10°C/min. X-Ray powder diffraction (XRPD) analysis of the crystal structure and Ca-P phases identification of the synthesized powders were performed before and after heat treatment (Fig. 3''').

After electrodeposition, for collecting the nanowires (Fig. 1c), the membranes were rinsed with deionised water, air dried then dissolved with dichloromethane heated at 40°C [46] until being dried. The size and morphology of nanowires/nanotubes were investigated by scanning electron microscopy (SEM). SEM analysis was performed using the JSM-6460LA microscope (Jeol). A Transmission electron microscopy (TEM) was performed at 300 kV using a H9000NAR microscope from Hitachi (Scherzer resolution 0.18nm); TEM images and selected-area electron diffraction (SAED) patterns were performed to study and confirm the structure and morphology of nanowires at the nanometer scale.

3. RESULTS

Firstly, the cathodic part of cyclic voltammogram (Fig. 2) with a stabilization of the current density between -1.5 V and -2.2 $V/_{Ag/AgCl}$ enabled to confirm the electrochemical potentials window (corresponding to the diffusion level) allowing the HA electrodeposition with minimized secondary compounds formation between those two values. So, the desired potential range for HA electrodeposition may be comprised between -1,5 and -2,2$V/_{Ag/AgCl}$, before the hydrogen evolution reaction becomes dominant [47], indicated by a sharp increase in the cathodic current density beyond -2.2 $V/_{Ag/AgCl}$ [47, 48].

By varying the deposition parameters (Table 1), we obtained different thin films. Those films were submitted to an X-Ray diffraction analysis. The XRD patterns (Fig. 3', 3") showed diffraction peaks characteristic of gold at 2θ = 38.16°, 44.38° and 64.56° and corresponding to the substrate (gold coating on the disks) and close to 8.10°, 18.75° and 34.58° attributed to the stainless steel disks and adhesive band (stabilizing the disks). The identification of the other peaks was difficult because many calcium phosphates give 2 theta diffraction peaks in very close position. In absence of H_2O_2 (Fig. 3'a), only the substrate gave peaks with no identified calcium phosphates. In presence of 6 and 9% vol H_2O_2, calcium phosphates were detected. At pH 4.5, a peak at 11.70 °, identified as (0 2 0) plane of brushite (DCPD, $CaHPO_4{\cdot}2H_2O$, *ICDD* file n° 009-0077) and one of the two more intense peaks of its XRD pattern could be seen in constant potentiostatic mode (Fig. 3'd, 3"e) but absent in pulsed potential mode (Fig. 3"f). At pH 6.0, whether constant or pulsed mode, no peak at 11.7° was present (Fig. 3' a, b, c; fig 3" g, h). All other diffraction peaks could be assigned to HA or OCP according to the standard database respectively *ICDD* file n° 009-0432 and *ICDD* file n° 079-0423 or to CDHA; their X-Ray patterns, very similar, may be confused. XRD patterns show broad and small peaks, larger at pH 4.5 (Fig. 3'd) than at pH 6.0 (Fig. 3'c). The peaks are narrower and have a higher intensity

in pulsed mode compared to constant mode for films deposited at pH 4.5 (Fig. 3"f> e), and at pH 6.0 (Fig. 3" h>g) in the studied potentiostatic mode. It was the same observations by applying a current density (data non presented). Finally, in the best conditions for obtaining HA deposits, we may have synthesized HA, CDHA, OCP or a mix of these phases. The strongest peaks were identified, their position at about 25.9°, 31.8°, 32.2° and 32.9° correspond respectively to the (0 0 2), (2 1 1), (1 1 2) and (3 0 0) planes of HA or could correspond to peaks of OCP.

Without H_2O_2, thin films (Fig. 3'a) were usually difficult to obtain, so no Ca/P molar ratio could correctly be measured. The Ca/P molar ratios of thin films (Fig 3.) were comprised between 1.46 and 1.74. Thin films obtained at pH 4.5 (Fig. 3'e) or 4.8 (Fig. 3"d) with 9% vol H_2O_2 in constant mode were associated to a Ca/P ratio of 1.46. At pH 4.5 with 9% vol H_2O_2 but in pulsed mode Ca/P ratio was 1.52 (Fig. 3"f). At pH 6.0, with 6% vol H_2O_2 in constant mode the Ca/P molar ratio was 1.53 (Fig. 3'b) and with 9% vol H_2O_2 in constant mode, the Ca/P molar ratios were 1.57 and 1.74 in constant mode for the 2 different samples realized in the same conditions (respectively Fig. 3'c and 3"g). In summary, in the best conditions, at pH 6.0 with 9% vol H_2O_2 and pulsed mode (Fig. 3"h) the Ca/P molar ratio was 1.55.

Powders, obtained from the crushing of thin films obtained in the best conditions of HA electrodeposition (pH 6.0, 9% H_20_2, pulsed mode (with t_{ON} = 1 min at E = -1,6V/$_{Ag/AgCl}$ and t_{OFF} = 2 min at E = free potential) for a 15 minutes effective deposition time) were submitted to a X-Ray diffraction analysis for identifying the electrodeposited materials. The obtained XRD patterns (Fig. 3''') showed diffraction peaks at 2θ = 38.16°, 44.38° and 64.56° characteristic of gold from the deposited layer. All other diffraction peaks could be assigned to HA (or CDHA) compound with absence of OCP owing to that the most intense characteristic (0 0 1) diffraction

peak at 2θ = 4.74° was not observed, respectively to the PDF database files JCPDS 009-0432 and JCPDS 079-0423 of these HA and OCP compounds. So, the XRD patterns revealed that the deposits were composed of HA or CDHA. The X-ray diffraction patterns of powders (XRDP) showed the typical peaks of HA/CDHA; the strongest peaks were found at about 2θ = 10.82°, 25.88°, 31.77°, 32.19° and 32.90° corresponding respectively to the diffraction on the (1 0 0), (0 0 2), (2 1 1), (1 1 2) and (3 0 0) crystallographic planes of HA (Fig. 3’’’).

In order to confirm the absence of OCP, we have submitted to an annealing (850°C-2h - N_2 flow), the powders issued from the crushing of thin films, based on Karampas *et al.* works [45, 49]. After heat treatment, the XRD spectra (Fig. 3’’’) revealed, the intense peaks of 3 phases: gold (coming from the sputtered gold coating weakly adhering to the stainless steel disks), HA and β-TCP whose six more intense peaks not assignable to HA are at 2θ = 13.56°, 27.75°, 30.98°, 34,30°, 46.91° and 52.99° (JCPDS 09-0169).

Before starting the template method, we controlled the thickness for one non-deposited polycarbonate membrane with 200 nm pores diameter on a cross sectional SEM view of this one (Fig. 4’) The measured value was 15.5 µm which allowed us to suppose that the 11 µm nominal thickness indicated by the society was not correct or inhomogeneous.

Although pulsed deposition produced the thickest and a more uniform coating in thin film, deposition in polycarbonate membrane occurred mostly at the periphery of the substrate rather than in its center (Fig. 4”a). Moreover, we often observed a rupture of the membranes in this peripheral zone (Fig. 4””a) and an inflation (Fig. 4”b). A metallic grid was interposed between the gold covered membrane (cathode) and the stainless steel disk cathode, in order to improve the electrical contact. With this grid, we have extended the deposition to all the membrane surface (Fig. 4”c) and prevented the membrane to break and to inflate as observed by optic microscopy (Fig. 4”d).

SEM micrographs showed that the 300 nm thickness gold coating evaporated on any membrane left the pores open (whatever its nanopores diameter) (Fig. 5a). Gold layer entered the first nanometers of pores and deposited on the nanopores walls without closing them completely as seen on SEM micrographs (Fig 5b). Imperfect (because of porous walls) nanotubes (Fig. 5 c, f) have been synthesized at -1,6 $V/_{Ag/AgCl}$, respectively from membranes with 100 nm pores diameter (Fig. 5 d, f) and 400 nm pores diameter (Fig. 5c) in pulsed mode (15 min effective deposition time, deposition time 1 s, break time 2 s). Nanotubes and nanowires could also be simultaneously synthesized as it could be seen from a sample with a deposition carried out in constant mode during 30 minutes at -1,6 $V/_{Ag/AgCl}$ (Fig. 5e).

Nanowires, obtained with the three different membranes, were observed by SEM on silicium wafers after membrane dissolution. The micrographs (Table 2) showed heaps of nanowires viewed on their length. The presented nanowires were produced by pulsed potential (-1.6 $V/_{Ag/AgCl}$) in membrane with pores diameter of 100, 200 and 400 nm during different time.

With the 100 nm pore size polycarbonate membrane, the aspect ratio of nanowires (diameter/length ratio) were in the range of 20 to 43 for 3 minutes and 37 to 71 for 5 minutes effective deposition duration with a final diameter comprised between 220 and 350 nm going until 3.5 times higher than original pores diameter. The aspect ratios of nanowires obtained in 200 nm pore size polycarbonate membranes were in the range of 19 to 22 for an effective 5 minutes' deposition time and 21 to 53 for an effective 15 minutes' deposition time. Their diameters measured 270 or 370 nm, i.e. until 1.8 times the original pores diameter. Others nanowires, obtained in membranes with a 400 nm pore diameter, presented an aspect ratio comprised between 10 and 19 for 5 minutes and between 9 and 25 for 15 minutes effective deposition time. Their average diameters started from 590 to 970 nm corresponding to a nanopores expansion going from 1.5 to 2.4 times.

The nanowires observed by TEM were obtained in the best conditions of synthesis (pH 6.0, 9% H_2O_2 and pulsed mode with t_{ON} = 1 min and t_{OFF} = 2 min) with pulsed potential at -1,6 $V/_{Ag/AgCl}$ (Fig. 6) and pulsed current density at -120 mA/cm² (Fig. 7) in a membrane whose pores diameter was 200 nm and with pulsed potential in a membrane with 400 nm pores diameter (Fig. 8). The TEM micrographs of the nanowires (constituted of nanoneedles) are presented (Fig. 6.a, 6.b, 7.a, 7.b, 8.a and 8.b) with the related selected area electron diffraction (SAED) patterns (Fig. 6.d3, 6.d4, 7.d1'', 7.d2 and 8.d3''). Those patterns present two intense partial rings of electron diffraction spots with distances of 0.33 nm and 0.27 nm corresponding respectively to the diffraction on (0 0 2) and (2 1 1) crystal planes of an apatite-like structure. The observation at high magnification (Fig. 6.V3-60K,6.V3-400K, 7.V1-500K, 7.V1-400K, 7.V2'500K and 8.V3-400k') of less contrasted zones in the heart of nanowires let appear the sequences of stacked crystalline planes. The interplanar spacings were measured on high magnification images with a periodicity of 0.34 nm along the longitudinal axis (Fig. 6.V3-400K, Fig. 7.V1-500K and Fig. 8. V3-400k') and 0.82 nm along a transversal axis (Fig. 7.V1-400K and Fig. 8. V3-400k') of the nanoneedles which are respectively consistent with the [0 0 1] and [1 0 0] directions of HA. Moreover, the Fourier Transform of a squared area of one nanoneedle (Fig 7. FT) is consistent with the simulated electron diffraction pattern of HA structure along the [0 1 0] zone axis (Fig. 7. $SEDP_{HA}$).

We can observe on TEM micrographs at moderate magnification the opacity of 1D structures obtained from membranes with 200 nm pores diameter (Fig. 6.a, 6.b, 7.a, 7.b) and the transparency of 1D structures obtained from membranes with 400 nm pores diameter (Fig. 8.a, 8.b). The nanoneedles constituting the 1D structures from membranes with 200 nm pores diameter were roughly uniaxially oriented in the longitudinal axis of nanowires (Fig. 6.a, Fig. 6.V3-60k, Fig.7a) whereas nanoneedles constituting 1D structures from membranes with 400 nm pores diameter were multiaxially oriented (Fig. 8.a, 8.b).

4. Discussion

The nanowires were produced in this study by a template-assisted electrodeposition; this template method involved the synthesis within the pores of a nanoporous membrane. The advantage of the template method is based upon nanowires being generally the exact replica of nanopores in diameter and length in a polycarbonate membrane. This nanowires synthesis never realized before makes possible a fast production of calibrated nanowires with a predetermined size and morphology. Nanowires length, diameter and amount can be modulated by the choice of the membrane characteristics: respectively thickness, diameter and density of nanopores. The performance of HA particles could thus be optimized for many applications and the homogeneity of the nanowires that we produced could give us hope that future experiments concerning the mechanical or biological properties of these compounds will be reproducible.

Our study is the first in which CaP nanowires are produced by pulsed electrodeposition in polycarbonate membranes. It is the second study applying a pulsed potential for a CaP electrodeposition [35] and the third time that calcium phosphates are electrodeposited on gold substrate [50, 51]. This synthesis employed aqueous baths, ensuring toxicity-free producted compounds, developed by Shirkhanzadeh *et al.* who succeeded, as early as 1991, to produce CaP deposits by electrodeposition [52]; in our work, hydrogen peroxide has been added.

Knowing that the quantity of nanowires produced by the template method would be too limited to perform physicochemical analyses, the optimal depositional conditions were determined by the deposition of thin films on gold obtaining a sufficient quantity for its characterization and keeping the same electrochemical conditions.

The deposits (in thin films and membranes) have been performed at a temperature of 70°C based on many works that have demonstrated crystalline HA formation at a temperature

comprised between 60°C [35, 53] and 85°C [54]. Electrolyte pH affects also directly the nature and crystals size of CaP phases [42]; Montero *et al.* highlighted that crystals size decrease with increasing pH for reaching a nanometer size at pH 6. In mostly studies [33, 36], deposition in acid baths, with pH range from 4 to 6, favours OCP formation with less crystallized deposition. Its nucleation and growth would be kinetically more favourable under physiological conditions [1]. But the more the pH reaches a weak acidic value between 6 and 7.4, the more HA is present until being the only phase [33, 36]. So, usually a higher pH favors monophasic and nanocrystals HA formation [33, 36] but electrodeposition often results in deposition of other calcium phosphates: OCP, β-TCP (β-$Ca_3(PO_4)_2$, whitlockite) or DCPD ($CaHPO_4 \cdot 2H_2O$, brushite) more probably because of lower pH generated at the cathode. In our bath, with adding NaOH for increasing the pH, an intense precipitation occurred which can disturb electrodeposition in nanopores. A compromise was found by choosing a weak acidic solution with an effective pH 6.0, sufficiently high to enable alone HA formation and not too high to prevent an important precipitation before electrodeposition.

In this work, at pH 4.5 and constant mode, brushite formation was favoured; one of its two intense XRD peaks at 2 theta = 11.7° was identified in the two samples obtained in this condition (Fig. 3'd and 3"e). With a Ca/P ratio of 1.0 for brushite and a Ca/P ratio of 1.67 for stoechiometric HA, the Ca/P molar ratio of 1.46 for this two samples (Fig.3'd and 3"e) corroborates the presence of brushite together with HA. Whereas at pH 6.0, all XRD peaks found were identified as HA or CDHA peaks (Fig. 3'b, 3'c, 3"g, 3"h, 3''').

In aqueous baths, the cathodic reduction of water, dissolved oxygen and phosphates groups results in a local and fast pH increase at the cathode's surface due to the generation of OH^- ions, inducing a nucleation on the cathode. But the electrochemical deposition has the disadvantage to generate H_2 bubbles that start evolving from the cathode surface [35, 39], lead to the

formation of volcano structures [54] and can prevent further CaP deposition (nucleation and growth). Our study, confirming partially the conclusion of many authors [34, 39], revealed a better CaP deposition in presence of 6-9% vol H_2O_2 (Fig. 3'b, c, d) and the best with pulsed mode (Fig 3''h); the obtained thin films were composed of CDHA. In some studies, the addition of 9% H_2O_2 could even lead to monophasic HA instead of CDHA with 6% H_2O_2 [34, 39]. Hydrogen peroxide (H_2O_2), recognized preventing bubbles formation (and/or favouring ions OH^- production), has the advantage to increase the pH leading to the predominant formation of the HA phase.

CDHA thin films after pulsed deposition [34, 35, 39] were previously found more crystallized, more uniform, denser and more adherent compared to their counterpart obtained in intentiostatic constant modes. LeGeros [55] was able to deposit CDA directly by pulsed ECD and in many studies, pulsed ECD associated with H_2O_2 leads to dense and uniform monophasic HA coatings [35, 39]. In pulsed mode, the relaxation time between two deposition times strongly reduces H_2 bubble emission and gives the calcium and phosphate ions in the solution sufficient time to diffuse to the cathode surface [34, 56]. The generated hydrogen may have time to escape [56]. Our XRD analyses (Fig. 3) showed that electrodeposited coatings in pulsed mode were composed of a CaP phase with typical diffraction peaks corresponding to HA / CDHA apatite-like structure (JCPDS 09-0432) (Fig. 2). It has also been described by many authors that pulse deposition gives rise to smaller crystallites (HA nanoparticles) than continuous deposition does [56]. This factor logically favors the nanowires formation.

So, in this work, benefits of 6 – 9% H_2O_2, pH 6.0 and pulsed mode, enabling the exclusive formation of HA (and/or OCP) in more homogeneous and denser deposits, were confirmed in thin films by XRD analyses (Fig. 3h). These conditions have generated narrower and higher XRD peaks than others conditions (0% H_2O_2, pH 4.5 and constant mode) did (Fig. 3), confirming a higher crystallinity and/or a higher amount of these deposits. Those observations

explained why in the present study, pulsed electrodeposition and an optimal quantity of H_2O_2 in electrolyte were combined for the nanowire synthesis.

XRD patterns of our thin films were more in favour of a hydroxyapatite or a calcium-deficient hydroxyapatite but XRD peaks that remain wide and with low intensity could also testify the presence of nanocristals or HA films with low crystallinity. There is also a possibility of misidentification between OCP and HA when using only the X-ray diffraction analysis at high angle ($2\theta > 10°$) because of their similarity in structure [57]. There is an extended overlapping between the peaks of OCP and HA especially in the region 25° and 31-33° where the peaks are of higher intensity corresponding respectively to the (002) plane and a combination of the (211), (112) and (300) planes of HA [49]. The main difference that may be able to distinguish OCP from HA is the most intense characteristic diffraction peak of OCP at $2\theta = 4.7°$ corresponding to the diffraction by the (100) crystallographic plane and additionally its two diffraction peaks at $2\theta = 9.4°$ and 9.8° corresponding respectively to the diffraction by the (110) and (010) planes of its structure (according to the PDF file JCPDS 079-0423) that we have never observed [33, 36] (Fig. 3). A reason for explaining why these peaks could be too small for being observed, could come from a highly textured coating with a particular crystalline orientation or could also be hidden by the background; but after crushing thin films in powders, no peak at 4.7°, 9.4° and 9.8° were detected (Fig. 3’’’) that was in favour of the absence of OCP. Distinction between CDHA and HA nanocrystals [3] is also complicated with lower and broader XRD peaks than those of stoichiometric HA. Pulsed mode at pH 6.0 with 9% vol H_2O_2 gave the best results in term of composition, crystallinity and amount of deposition but our methods of characterization (analyses by XRD (Fig. 3)), Raman and Infra-red spectroscopies) appeared to be insufficient to determine the exact composition of the electrodeposited materials. In the SAED patterns (Fig. 6, 7 and 8), although OCP presents, at low diffraction angle, intense reflection corresponding to the diffraction by the (100) plane at distance of 1.9 nm that makes able to clearly distinguish

OCP from HA, it was not possible to observe this diffraction spot because of its absence or especially because of the occultation by the beam-stop and the highly intense spot of the direct beam which make it difficult to observe.

There was the same problem of peaks overlapping in the X-Ray diffractogramms and in Infra-red or Raman spectra for thin films. A method described by Karampas *et al.* was transposed to our samples [45]. The CaP powders obtained by crushing two thin films obtained after 15 minutes effective deposition time (realized in the best and the same conditions than for nanowires) were submitted to a heat treatment, at 850°C during 2 hours, in order to determine OCP presence (Fig. 3’’’). It is well accepted that stoichiometric HA heat treated up to 1200°C keeps its crystallographic structure [45, 58] because it’s the most thermodynamically stable CaP phase; on the contrary, the instable OCP converts into β-TCP (beta tricalcium phosphate, JCPDS 09-0169) and β-CPP (calcium pyrophosphate, β-$Ca_2P_2O_7$, JCPDS 01-071-2123) [49]. Some studies have highlighted the transformation of poorly crystalline CDHA in a biphasic mixture of HA and β-TCP during calcination at temperature close to 800°C [58, 59]. After heat treatment, XRD analysis (Fig. 3’’’) revealed that powders were composed of three compounds: gold (coming from the gold film sputtered on stainless steel disks), HA and β-TCP identified by their characteristic peaks. Although the SAED patterns (Fig. 6, 7 and 8) could also be controversial for phase identification because their spacing values (0.34 and 0.28 nm) exist both in HA and OCP [60], the XRD analysis of the heat-treated powders indicating the absence of β-CPP and presence of β-TCP, coupled to the Ca/P ratio of 1.55 in the same conditions (pH 6.0, 9% vol H_2O_2 and pulsed mode) (Fig. 3”h) , enabled us to conclude on the absence of OCP and that the original thin films were composed of CDHA whose apatite-like structure was the only crystalline phase observed by TEM (Fig. 6, 7 and 8); So it could logically be thought that the composition of the nanowires is the same as this of thin films in the same electrochemical

conditions. This confirms the description of other authors [8, 36] saying that HA can be the only component in weak acidic conditions and the results of Lu who declared that the CDHA formation is favoured in aqueous solutions [1]. In our thin films, an amorphous phase (ACP), whose presence was suggested by a perturbated background on X-ray diffractograms [53, 61], could explain Ca/P ratios higher than 1.67 (Fig. 3"g) but some residues of $Ca(OH)_2$ coming from reaction between OH^- and Ca^{2+} ions could also explain it. The XRD peaks, generally broad, could be attributed to a poor crystallinity, residual strain [62] or a nanocrystalline structure [2].

A Rietveld refinement of the X-Ray diffraction patterns of the heat-treated powders (obtained from crushing of thin films deposited during 15 minutes effective duration) was realized for a quantitative evaluation of composition. The fractions of β-TCP and HA found were very similar for the two conditions: 69.0 and 31.0% weight respectively in pulsed intentiostatic mode (- 120 $mA.cm^{-2}$) and 69.5 and 30.5% weight respectively in pulsed potentiostatic mode (-1.6V/$_{Ag/AgCl}$). Many authors have remarked that the obtained compounds are dependent on the initial Ca/P ratios of the precursors and that HA/β-TCP ratio is determined by the initial calcium-deficiency and sintering temperature [63]. A higher proportion of β-TCP is indicative of an increased calcium deficiency of the original CDHA (before calcination) [64]. In parallel, the Ca/P ratio of the initial CDHA can be calculated by determining the phase proportions in the calcined biphasic materials and inversely the proportion of β-TCP/HA of the calcined compounds can be estimated from the Ca/P ratio of the non-heated powders [64]. With the help of the Rietveld Refinement, by knowing the ratio of HA/β-TCP, we could easily deduce the Ca/P ratio of the original thin films (before heat-treatement). This average composition gave an estimated value of the expected Ca/P ratio of the original thin films of 1.55 that corresponded very closely to the Ca/P ratios' values of our thin films estimated by EDX spectroscopy (1.55 (fig. 3"h) and 1.52 in potentiostatic and intentiostatic modes respectively), enabling to

corroborate the conclusions of the heat treatment saying that thin films were composed of CDHA whose Ca/P ratio (between 1.33 and 1.67) is smaller than the theoretical value of stoichiometric HA (1.67). For memory, the Ca/P value of OCP is 1.33 and that of ACP ranges from 1.0 to 2.0. The absence of other elements (possible carbonates or sodium atoms) detected by spectroscopic studies enabled us to conclude that CDHA synthesized was not substituted.

These optimized conditions for synthesizing on gold a calcium-deficient hydroxyapatite (CDHA) in dense and homogeneous thin films were transferred to the nanowires synthesis on gold covered polycarbonate membranes.

Generally, an intentiostatic mode is preferred instead of a potentiostatic mode because of a better deposition process control and generally denser and thicker deposits. Our results also corroborate the suggestion of Han *et al.* [65] saying that a high current density can increase ions quantity deposited with a competition of crystalline growth inducing a slower growth and explaining smaller crystals size [55] and a more dense and uniform structure. In many studies [61], OCP is obtained at weak current density and monophasic nanoparticles HA coatings at high current densities: between 50 and 240 $mA.cm^{-2}$ [40, 41, 42] even if some authors have obtained HA with low current density (such as 1 $mA.cm^{-2}$) [66]. It is recognized that applying a high current density during pulsed electrodeposition gives a greater cathodic potential (greater than $-2V_{/SCE}$) conducting to a favorable higher pH in the vicinity of the cathode. A potentiostatic mode was also tested because it is impossible to exactly determine the real active surface area of membranes. Because of H_2 bubbles progression into some pores, the surface area could be reduced and this gives to a non-determinated part of the surface a non-conductivity.

It was remarked the best results in term of crystallinity, density, homogeneity and only presence of CDHA for a potential close to $-1.6\ mV/_{AgAgCl}$. This potential value was chosen because of its localization inside the electrochemical potential window (Fig 2). The current density registered

for this potential was comprised between -65 and -90 mA/cm for thin films (Table 1) whereas it was comprised between -120 and -300 $mA.cm^{-2}$ for depositions in polycarbonate membranes (Table 2).

After electrodeposition, in agreement with Blackwood works on thin films [56], a more abundant deposition on polycarbonate membrane was mostly observed at the substrate periphery rather than at its center along with a distortion of the membranes (Fig. 4''a), possibly due to edge effects which generate also a greater hydrogen evolution. Hydrogen bubbles can pass through the porous and weak membranes and this can explain why we found the membranes inflated and ruptured all around the periphery resulting in isolation from the cathode (Fig. 4''c). Other reasons could be the impregnation of the membrane by the bath, the possible diffusion through the membrane of this one that inflates with temperature and the stresses exerced by a current applying. With a metallic grid interposed between the membrane and the cathode, the membrane doesn't inflate (Fig. 4''d), the electrical contact is enhanced and the deposit obtained is more uniform (Fig. 4''c); we have extended the deposition to the entire surface of the membrane and surely gained in quantity of nanowires.

Because the amount of produced nanowires was too low to be analysed by XRD, they were observed by SEM microscopy and a TEM analysis was realized for assessing the presence of apatite. The physical (shape, size and distribution of the pores) and chemical (composition and functional groups on surfaces) properties of the membranes are considered as the main factors for controlling the size and morphology of the products**.** The polycarbonate membranes contain cylindrical and non-connected nanopores, with mono-dispersed diameters, which extend through their entire thickness. After their dissolution in dichloromethane heated at 40°C,

nanowires could be distinctly observed on micrographs in Table 2 signifying the success of the template-assisted electrodeposition. The obtained HA nanowires had an almost uniform length and diameter.

The nanowires diameter is predetermined by the nanopores diameter and their length can be controlled by the duration of electrodeposition but the average length and diameter of the nanowires seen on SEM micrographs (Table 2) didn't correspond exactly to those of nominal nanopores. We observed for all the membranes, an increasing length of nanostructures (nanowires/nanotubes) with deposition time (Table 2). The maximum length to obtain corresponded logically to the membrane thickness but the longest nanowires were curiously longer than expected as Zhang [67] could observe it with metallic nanowires. In our study, the longest produced nanowires measured 15.9, 14.5 and 15.6 µm for the membranes with 100, 200 and 400 nm nanopores diameters respectively suggesting that the membranes were thicker than the thickness value declared by the fabricant (11µm) and were close to 16 µm. This hypothesis was most likely after the thickness measurement of 15.5 µm determined by SEM on membrane cross-sections (Fig. 4). The thickness of the membranes may also not be perfectly constant or owing to the random nature of the pore-production process, all pores may not be of the same length than the membrane thickness because the angle of the pores with respect to the surface could be as large as 34° [68]. This last hypothesis was refuted by the SEM observation of nanopores close perpendicular to the surface of the membrane in a cross-sectional view (Fig. 4'). But some nanowires produced during the same duration, were shorter (Table 2). This could be explained by the explanation of Blackwood [56] with the fact that a constant deposition by potentiostatic method could be hard to control because as the dielectric Ca-P forms, a potential drop could occur leading to a decrease of the deposition rate during the experiment. By a mass transport limitation or an ohmic drop generated by the electrolyte, potential can also

decrease and stop the nanowires growth. It could also be explained by a progression of H_2 bubbles that blocks the synthesis or because the nanowires randomly break as a result of the presence of defects and their intrinsic weakness [67]. With metallic nanowires, Keating stated that particles with aspect ratio above 25 are susceptible to breakage [69].

Finally, we observed (Table 2) the entire filling of nanopores after 5 and 15 minutes of effective deposition for membranes respectively with 100 and 200 nm nanopores diameters enabling to obtain nanowires with respective aspect ratios of 37 to 71 and 21 to 53. For membranes with a 400 nm pores diameter, 10 minutes enabled to obtain nanotubes with the maximal length close to 16 µm and an aspect ratio from 9 to 25. Increasing deposition time with this last membrane didn't lead to the filling of nanotubes with nanowires formation but the weakness of the membranes after some time in electrolyte limited often proper observations.

The nanowires diameters could measure up to 3.5 and 1.8 fold the original pores diameters for membranes respectively with 100 and 200 nm pores diameters. The nanotubes external diameters were up to 2.4 fold wider than the original pores diameter for membranes with a 400 nm pores diameter. Current density does not appear responsible of these nanopores enlargement because the same observations were made whatever the current density (Table 2). So, this could occur because of a widening of the nanopores during electrodeposition, either by a radial growth of the CaP nanostructures (exerting pressure on the membrane such as Schönenberg could explain it with metallic nanowires), by pressures exerted by heated bath [46] or by a thermal expansion of the whole membrane. An other probable reason is the possible H_2 bubbles that form at the cathode and dilate pores. The nanowires have a uniform diameter on the totality of the length (Table 2). The aspect ratios (L/D) have ranged from 9 to 71 among the nanowires obtained (Table 2). The most interesting aspect ratio (37-71) was logically obtained for nanowires in the membrane whose pores have the smallest diameter (100 nm)

followed by the nanowires obtained in membranes with 200 nm nanopores diameter with an aspect ratio from 21 to 53 and finally the smallest aspect ratio (9-25) was obtained for nanowires synthesized in membranes with 400 nm nanopores diameter (Table 2).

A TEM observation (Fig. 6, 7 and 8) completed the structural study of the nanowires. The presented nanowires were obtained in the two best conditions of synthesis (pulsed potential at -1.6V $_{/AgAgCl}$ (Fig. 6) and pulsed current density at 120 $mA.cm^{-2}$ (Fig. 7)) in a membrane with 200 nm pore diameters. TEM observations confirmed the other analyses; SAED patterns and TEM micrographs showed respectively that CaP nanowires are polycrystalline and constituted by an entanglement of needles oriented along their longitudinal axis (Fig. 6.a, 6.V3-60k, 6.b, fig 6.a, 6.b). TEM micrographs at high magnification obtained at 300 KV showed that the nanoneedles were crystallized because of an identified periodicity of the crystalline planes stacking (Fig. 7.V1-500k, V1-400K, V2'-500k). Moreover, the observation of less contrasted zones suggests that the core of nanowires is also crystalline (Fig. 7.V3-400k). We have not distinguished significant differences between the two samples (Fig. 6 and 7). The selected area electron diffraction (SAED) patterns (Fig. 6.d3, 6.d4, 7.d1'', 7.d2) revealed polycrystalline state with the main intense reflexions corresponding to the distances of 0.34 nm and 0.28 nm respectively characteristic of the diffraction by the (0 0 2) and (2 1 1) planes of an apatite-like structure. The periodicity of the stacked crystalline planes measured from Fourier Transform pattern (Fig. 7.FT) and TEM micrographs at high magnification (Fig. 6.V3-400K, 7.V1-500K, 7.V1-400K) is consistent with a HA or CDHA phase and the interplanar spacing along the longitudinal axis of nanoneedles was measured with a periodicity of 0.34 nm corresponding to the interplanar distance of the (002) planes of HA. These observations confirmed the apatite-like structure of the nanowires and that the growth orientation of nanoneedles (oriented preferentially along the longitudinal axis of nanowires (Fig 6.V3-60k, Fig. 7a) corresponds to

the < 0 0 1 > crystalline orientation of HA (c-axis) that is the preferential growth orientation of HA 1D nanostructures [67].

This observation is in good accordance with the works done by Ferraz who observed that monocrystalline HA nanocrystals synthesis occurs below 60°C and that above this critical temperature, the synthesis leads to polycrystalline form [70]. Xiao also declared that nanowires synthesized using a template-directed method in porous materials are usually polycrystalline [71]. We can hypothesize that the crystalline nanoneedles constituting the nanowires are formed in the first mechanism of nucleation on the cathode [38] and are the same identified by SEM in the sublayer of needles observed in our thin films. Wang *et al.* [72] observed two distinct layers in HA electrodeposited films which supported the occurrence of two distinct nucleation mechanisms suggested by Eliaz *et al.* [38]. The latter have assumed that deposition starts with a two-dimensional growth (instantaneous mechanism) and changes after a few minutes for a three-dimensional growth (progressive mechanism). In our work, many coatings were composed of two layers of particles distinguishable by their morphology: on the top, microsized spheroids formed by a needles agglomeration [34, 53] with a sub-layer of dispersed nanoneedles [53]. Thirsk *et al.* [73] consider to the contrary that 2D and 3D growths can indifferently be issued from gradual or instantaneous nucleation.

The analyses by TEM micrographs (Fig. 8a, 8b) and SAED patterns (Fig. 8d3'') of nanostructures produced in membrane with 400 nm pores diameter enabled also to conclude to their polycrystalline and apatitic nature with the entanglement of nanoneedles. The periodicity of the stacked crystalline planes measured in the longitudinal axis of the nanoneedles (Fig. V3-400k') (0.34 nm) corresponded also to the interplanar distance of the (002) planes of HA. To

the contrary of nanowires obtained in nanopores of 100 and 200 nm diameters, with membranes of 400 nm nanopores diameter, the nanostructures were constituted by randomly entangled nanoneedles, not oriented along the longitudinal axis of nanowires. We could also better distinguish the nanoneedles inside those structures because of a higher transparency to the electron beam (Fig. 8.a, 8.b) compared to the nanowires (Fig. 6a, 6b, 7a, 7b) at similar magnification. TEM (Fig. 8a, 8b) combined to SEM observations (Table 2) of structures more porous than nanowires obtained from nanopores of 100 or 200 nm diameters helped us to conclude that nanotubes were synthesized in membranes with 400 nm nanopores diameter. The possibility to obtain nanotubes was confirmed by many SEM observations (Fig 5).

Growth in pores is recognized to be more complex that in thin films. Many authors [46, 44, 74] have highlighted that electrochemical behaviour with formation of nanotubes or nanowires is dependant on many parameters such as current density, electrodeposition duration [68, 76], potential waveform, growth rate [44], nanopores size (diameter and aspect ratio [74]). For example, Yoo *et al.* [75] observed for metal nanostructures and anodized aluminum oxide membranes with weak current density that metal electrodeposited slowly and preferentially on cathode surface producing nanowires by a bottom-up growth phenomena i.e. a layer by layer growth from bottom along the nanopores direction whereas a higher current density was accompanied by a wall-surface growth pattern because the high electric field concentrated at the edge of nanopores and preferential electroplating occured through the surface of nanopores [75]. In an other study in polycarbonate membrane, diffusion coefficient appeared dependant on nanopores size [46] explained by a probable viscosity change of electrolyte inside pores. Hydrodynamics motions of electrolyte are necessarily different under the different nanopores diameters [46]. Martin [76] and Ertan [74] affirmed that a short deposition time could generate

nanotubes and a longer time, nanowires. Nanowires growth mechanism was also described by Li *et al.* [77] as a brick-stacked wirelike growth with bricks stacking along the direction of nanopores from the bottom to the top of membrane.

From our study we can guess and explain the nanopores filling mechanism. Nanopores were never closed on their bottom (Fig 5a) by the gold covering (whatever 300 nm or 1 µm of gold thickness) which generated a gold ring around nanopores (Fig 5.b). Gold could penetrate and deposit on the first nanometers of nanopores walls as it could be seen on SEM micrographs (Fig 5b). This gold ring acts as a preferential nucleation site.

H_2 bubbles progression inside nanopores that physically pushes CaP material against the nanopores walls [44] could explain why we had found simultaneously nanowires and nanotubes in a same sample (Fig. 5e). But others parameters could also explain the nanotubes formation; an insufficient current density proposed by Hulteen [68] could explain why we observed nanotubes with eventually porous walls in membranes with 100 nm pores diameter (Fig 5d, 5.f) or 400 nm pores diameter (Fig. 5c). Effectively those nanotubes were obtained in pulsed mode with deposition time 1s and break time 2s. Our observations of nanowires with membranes of 100 and 200 nm nanopores diameters and nanotubes with membrane of 400 nm nanopores diameter is consistent with the findings of Ertan, Liu *et al.* [74, 78]. They observed that nanopores with a high aspect ratio (close to 60 in their study) favours the nanowires formation with a layer by layer growth and a smaller aspect ratio (close to 11) favours nanotubes formation with a growth on nanopores walls enabling us to establish the mechanisms of nanopores filling (Fig. 9a, 9b). Our observations enabled us to suggest that nanoneedles growth in nanowire shape from the bottom to the top of membranes with a preferential orientation parallel to the long-axis of nanopores (Fig 9b') [77]; in this situation the role of gold ring seems to be major while

nanoneedles in nanotube shape seem to nucleate and growth preferentially on the pores walls (probably by adsorption) in a randomly orientation (Fig 9a').

A gold coating of 300 µm thickness on membranes with 400 nm nanopores diameter leaves on the bottom of nanopores non gold covered area wider than the ones on the bottom of 100 or 200 nm diameter nanopores. This could explain why the gold ring at the bottom of 400 nm diameter nanopores that act as a nucleation site enabled the nanotubes formation instead of nanowires formation. Spain [79] observed a phenomen corroborating the effect of gold ring; in polycarbonate membrane, metallic nanowires were synthesized when pores were closed by gold on the conductive side whereas nanotubes were synthesized when gold was removed from the bottom of the pores leaving just a gold ring.

In our study, the observation of nanotubes with porous walls (Table 2 and Fig. 5c, 5f) and an almost complete length (13.2 µm) after a short time (5 minutes) that has changed little with doubling time (Table 2) and the observation to the contrary of nanowires from narrower nanopores that were partially filled after 5 minutes, let us conclude that in this situation, the polycarbonate of nanopores walls have a highly significant role as nucleation sites. The preferential deposition observed along the nanopores walls could be due to an ions adsorption by electrostatic and ionic factors [80] such as the Van der Waals forces. Electrolytic ions could adsorb and preferential nucleation could be due to opposite charges. According to the idea suggested by Tourillon [81], a complexation of Ca^{2+} cations from calcium salts in electrolytic bath with carbonates functions ($-CO_3^{2-}$) of polycarbonate membrane could be possible and explain the preferential nucleation on nanopores walls.

The lines of electrical field may also be different with different nanopores diameters. The

gradient of electrolyte concentration that determinates many parameters such as diffusion current is also higher in narrower nanopores enabling to explain a different behaviour with membrane of high and low aspect ratio nanopores [74]. Cao explained a preferential deposition of materials on nanopores walls of a polycarbonate membrane with wider pores by a higher surface area providing more active sites (energetically favourable) for ions adsorption before their reduction [80].

5. Conclusion

Multiplicity of electrochemical deposition parameters had made difficult the obtention of CDHA alone in dense and well-crystallized thin films but we succeeded to determine the optimal conditions for CDHA synthesis on gold substrate. The different analyses carried out (XRD, Raman, FTIR and EDX spectroscopies, SAED, SEM and TEM) were not sufficient to determine the exact nature of the CaP phases. A heat treatment helped us to conclude that compounds in thin films were composed of one only crystalline phase of CDHA. By transferring the best conditions in polycarbonate membranes, we have succeeded for the first time in synthesizing high aspect ratio isolated CDHA nanowires (ranging from 19 to 71) by a template-assisted electrodeposition with a pulsed method in acidic aqueous baths (pH 6) composed of 0.042 mol.L^{-1} $Ca(NO_3)_2$ and 0.025 mol.L^{-1} $NH_4(H_2PO_4)$ with the presence of 9% H_2O_2. Nanowires were obtained with an applied potential of -1,6 $V/_{Ag/AgCl}$.

This pioneer method provides an efficient way to synthesize CDHA nanowires and nanotubes. It has the advantages of being a simple, inexpensive, green and fast method representing a high industrial interest. Moreover, it has a great capacity of control onto morphology and size that is missing in others methods of nanostructures synthesis and nanowires in particular. The length,

diameter and quantity of the nanowires can be controlled by the characteristics of the chosen membrane (thickness, pores diameter and pore density) but also by deposition duration and current density [44, 82]. The size of nanopores diameter controls also the morphology of 1D structures (nanotubes or nanowires) and would have a major role according to Ertan [74]. A TEM analysis highlighted that the produced nanowires and nanotubes were polycrystalline and constituted of nanoneedles with an apatite-like structure. A maximal length close to 16 µm was obtained for nanowires in 5 and 15 minutes of effective deposition time respectively for membranes with pores diameter 100 and 200 nm and in 10 minutes for nanotubes in membranes with 400 nm pores diameter. Produced nanowires have the advantage of a high aspect ratio (19-71) with calibrated size and synthesized nanotubes benefit from a high specific surface area [79] which compensates a lower aspect ratio (9-25).

By the same time, this study enabled to understand the mechanism of nanopores filling in polycarbonate membrane with preferential nucleation on gold in membranes with 100 and 200 nm nanopores diameter and growth along the longitudinal axis of nanopores, whereas a preferential and randomly nucleation on nanopores walls in membranes with 400 nm nanopores diameter corroborating the affirmation of Ertan *et al.* [74].

New processing of CDHA brings new opportunities to study its properties and interactions and consequently to understand its role in mineralized structures. Many studies [9, 15] confirmed that nanowires or nanotubes (of HA or CDHA in particular) by a high aspect ratio and a high specific surface area can mechanically and biologically reinforce matrices in bone substitutes but tested 1D nanostructures have generally a wide size distribution and a low aspect ratio.

We can easily affirm that the CDHA calibrated nanowires (or nanotubes) synthesized in this work will optimize the mechanical and biological performances of particles for bone substitutes. Furthermore, the homogeneity of the nanowires that we produced may make us

think that the mechanical or biological responses of future experiments will be more reproducible than with less homogeneous 1D nanostructures obtained by other methods. Their use and study will allow a better understanding of size and aspect ratio impacts for those properties and a better understanding of properties and behaviour of the materials at nano-, micro- and macroscopic scales.

REFERENCES

[1] Lu X, Zhao Z, Leng Y. Calcium phosphate crystal growth under controlled atmosphere in electrochemical deposition. J Cryst. Growth 2005;284:506-516

[2] Drouet C. Apatite formation: why it may not work as planned, and how to conclusively identify apatite compounds. Biomed Res Int 2013:490946.

[3] Mavropoulos E, Rossi AM, da Rocha NCC,Soares GA, Moreira JC, Moure GT, Dissolution of calcium-deficient hydroxyapatite synthesized at different conditions, Mater Charact, 2003;50:203-207

[4] Lin JHC, Kuo KH, Ding SJ, et al. Surface reaction of stoichiometric and calcium-deficient hydroxyapatite in simulated body fluid. J Mater Sci Mater Med 2001;12(8):731-741.

[5] Li H, Gong M, Yang A, Ma J, Li X, Yan Y. Degradable biocomposite of nano calcium deficient hydroxyapatite-multi(amino acid) copolymer. Int J Nanomed 2012;7:1287-1295

[6] Suzuki O, Kamakura S, Katagiri T, Nakamura M, Zhao B, Honda Y, Kamijo R. Bone formation enhanced by implanted octacalcium phosphate involving conversion into Ca-deficient hydroxyapatite. Biomaterials 2006;27:2671-2681

[7] Dorozhkin SV. A review on the dissolution models of calcium apatites. Prog Cryst Growth Charact. 2002;44(1):45-61.

[8] Shirkhanzadeh M, Azadegan M, Stack V, Schreyer S. Fabrication of pure hydroxyapatite coatings by electrocrystallisation and fluoridated-hydroxyapatite. Mater Lett 1994;18:211-214

[9] Balasundaram G, Sato M, Webster TJ. Using hydroxyapatite nanoparticles and decreased crystallinity to promote osteoblast adhesion similar to functionalizing with RGD. Biomaterials 2006;27:2798-2805

[10] Wu L, Dou Y, Lin K, Zhai W, Cui W, Chang J. Hierarchically structured nanocrystalline hydroxyapatite assembled hollow fibers as a promising protein delivery system. Chem Commun. 2011;47(42):11674-11676.

[11] Elias KL, Price RL, Webster TJ. Enhanced fuctions of osteoblasts on nanometer diameter carbon -fibers. Biomaterials 2002;23:3279-3287
[12] Shi Z, Huang X, Cai Y, Tang R, Yang D. Size effect of hydroxyapatite nanoparticles on proliferation and apoptosis of osteoblast-like cells. Acta Biomater 2009;5:338-345
[13] Zhang L., Chen Y, Rodriguez J, Fenniri H, Webster T. J., Biomimetic Helical Rosette Nanotubes and Nanocrystalline Hydroxyapatite Coatings on Titanium for Improving Orthopedic Implants. Int. J. Nanomed. **2008**;3:323–333.
[14] Sitharaman B, Shi X, Walboomers X.F, Liao H, Cuijpers V, Wilson L.J., Mikos A.G. and Jansen J.A.: In vivo biocompatibility of ultra-short single-walled carbon nanotube/biodegradable polymer nanocomposites for bone tissue engineering. Bone.2008; 43(2):362.
[15] Shen Y, Liu J, Lin K, Zhang W. Synthesis of strontium substituted hydroxyapatite whiskers used as bioactive and mechanical reinforcement materia. Mater Lett 2012;70:76-79.
[16] Zhang Y-G, Zhu Y-J, Chen F, Wu J. Ultralong hydroxyapatite nanowires synthesized by solvothermal treatment using a series of phosphate sodium salts. Mater Lett 2015;144:135-137.
[17] Corni I, Ryan MP, Boccaccini AR. Electrophoretic deposition: From traditional ceramics to nanotechnology. J Eur Ceram Soc. 2008;28(7):1353-1367.
[18] Webster TJ, Ergun C, Doremus RH, Siegel RW, Bizios R. Enhanced functions of osteoblasts on nanophase ceramics. Biomaterials 2000;21:1803-1810
[19] Müller FA, Gbureck U, Kasuga T, Mizutani Y, Barralet JE, Lohbauer U. J. Am Ceram Soc 2007;90(11):3694-3697
[20] Saito N, Usui Y, Aoki K, Narita, N et al. Carbon nanotubes : biomaterial applications. Chem. Soc. Rev. 2009, 38, 1897−1903.
[21] Kim G, Park B. Synthesis and growth mechanisms of one-dimensional strontium hydroxyapatite nanostructures. Inor Chem 2005;44:9895-9901
[22] Thomas Reardon PJ, Handoko AD, Li L, Huang J, Tang J. Dimensionally and compositionally controlled growth of calcium phosphate nanowires for bone tissue regeneration. *J Mater Chem B,* 2013, 1 (44), 6170.
[23] Costa DO, Dixon SJ, and Rizkalla AS, One- and Three-Dimensional Growth of Hydroxyapatite Nanowires during Sol − Gel − Hydrothermal Synthesis. *ACS Appl Mater Interfaces*, 2012, 4 (3), 1490-1499.
[24] Jiang, Zhu Y-J, Chen F, Wu J. Solvothermal synthesis of submillimeter ultralong hydroxyapatite nanowires using a calcium oleate precursor in a series of monohydroxy alcohols. Ceramics Int 2015;41:6098-6102
[25] Bose S, Banerjee A, Dasgupta S, Bandyopadhyay A. Synthesis, processing, mechanical, and biological property characterization of hydroxyapatite whisker-reinforced hydroxyapatite composites. *J Am Ceram Soc*, 2009, 92 (2), 323-330.
[26] Teshima K, Lee SH, Sakurai M, et al. Well-formed one-dimensional hydroxyapatite crystals

grown by an environmentally friendly flux method. *Cryst Growth Des,* 2009, 9 (6), 2937-2940.
[27] Lin K, Liu X, Chang J et al. Facile synthesis of hydroxyapatite nanoparticles, nanowires and hollow nano-structured microspheres using similar structured hard-precursors. *Nanoscale*, 2011, 3, 3052-3055.
[28] Zhang Y, Zhou L, Li D, Xue N, Xu X, Li J. Oriented nano-structured hydroxyapatite from the template. *Chem Phys Lett,* 2003, 376 (3-4), 493-497.
[29] Bean C. Process for filling Pores - United States Patent Office 3,483,095 [Internet]. [cited 12 sept 2017]. Available from:
https://docs.google.com/viewer?url=patentimages.storage.googleapis.com/pdfs/US3483095.pdf
[30] Possin GE. A method for forming very small diameter wires, review of scientific instruments 1970;41:772-774
[31] Masuda H, Fukuda K. Ordered metal nanohole arrays made by a two-step replication of honeycomb structures of anodic alumina. Science 1995;268(5216):1466-1468
[32] Wang S, Lei Y, Zhang Y, Tang J, Shen G, Yu R. Hydroxyapatite nanoarray-based cyanide biosensor Anal. Biochem 2010;398:191-197
[33] Eliaz N, Sridhar TM. Electrocrystallization of Hydroxyapatite and Its Dependence on Solution Conditions. Cryst growth des 2008;8(11):3965-3977
[34] Drevet ., Benhayoune H, Wortham L, Potiron S, Douglade JV, Laurent-Maquin D. Effects of pulsed current and H_2O_2 amount on the composition of electrodeposited calcium phosphate coatings. Mater Charact 2010;61:786-795.
[35] Chen X-Y, Zhao Z-W, Chen A-L, Li H-G. Pulsed electrodeposition of hydroxyapatite on titanium substrate in solution containing hydrogen peroxide. Surf coat technol 2007;l7:617-621
[36] Shirkhanzadeh M. Direct formation of nanophase hydroxyapatite on cathodically polarized electrodes. J mater Sci : mater med 1998;9:67-72
[37] Vijayaraghavan TV, Bensalem A. Electrodeposition of apatite coating on pure titanium and titanium alloys. J Mater Sci Lett 1994;13:1782-1785
[38] Eliaz N, Eliyahu M. Electrochemical processes of nucleation and growth of hydroxyapatite on titanium supported by real-time electrochemical atomic force microscopy. J Biomed Mater Res, 2007;80A:621-634
[39] Benhayoune H, Drevet R, Faure J, Potiron S, Gloriant T, Oudadesse H and Laurent-Maquin D. Elaboration of Monophasic and Biphasic Calcium Phosphate Coatings on Ti6Al4V Substrate by Pulsed Electrodeposition Current. Adv Eng Mater 2010; 12(6):B192-B199
[40] Narayanan R, Dutta S, Seshadri SK. Hydroxyapatite coatings on Ti-6Al-4V from seashell. Surf coat technol 2006;200:4720-4730
[41] Montalbert-Smith R, Montero ML. Formation of hydroxyapatite nanosized and other apatites by electrolysis process. Key Eng Mater 2009;396-398:579-582
[42] Montero ML, Saenz A, Rodriguez JG, Arenas J, Castan VM. Electrochemical synthesis of

nanosized hydroxyapatite. Mater Sci Lett 2006;41:2141–2144
[43] Lin D-Y,Wang X-X. Electrodeposition of hydroxyapatite coating on CoNiCrMo substrate in dilute solution. Surf coat technol 2010;204:3205-3213
[44] Inguanta R, Piazza S, Sunseri C. Influence of electrodeposition techniques on Ni nanostructures. Electrochimica Acta. 2008;53:5766-5773.
[45] KONTOYANNIS C, KARAMPAS I. Development of methodologies for characterization of calcium phosphates in their mixture. Proceedings of the 13th Panhellenic Pharmaceutical Congress; 2007 May 12-14; Athens, Greece. Available from:
http://nemertes.lis.upatras.gr/jspui/bitstream/10889/5186/1/PMO027.pdf
[46] Schönenberger C, Van der Zande BMI, Fokkink LGJ, Henny M, Schmid C, Krüger M, Bachtold A et al. Template synthesis of nanowires in porous polycarbonate membranes : electrochemistry and morphology. J Phys Chem. B 1997;101:5497-5505
[47] Eliaz N, Eliyahu M, Electrochemical processes of nucleation and growth of hydroxyapatite on titanium supported by real-time electrochemical atomic force microscopy. J Biomed Mater Res 80A: 621–634, 2007.
[48] Motoyama M, Fukunaka Y, Sakka T, Ogata YH, Kikuchi S. Electrochemical processing of Cu and Ni nanowire arrays. J Electroanal Chem. 2005;584(2):84-91.
[49] Karampas IA, Kontoyannis CG. Characterization of calcium phosphates mixtures. Vib Spectrosc. 2013;64:126-133
[50] Yang L, Wei W, Gao X, Xia J, Tao H. A new antibody immobilization strategy based on electrodeposition of nanometer-sized hydroxyapatite for label-free capacitive immunosensor. Talanta 2005;68:40-46
[51] Metoki N, Sadman K, Shull K, Eliaz N, Mandler D. Electro-Assisted Deposition of Calcium Phosphate on Self-Assembled Monolayers. Electrochim Acta 2016;206:400-408
[52] Shirkhanzadeh M. Bioactive calcium phosphate coatings prepared by electrodeposition. J Mater Sci Lett 1991;10(23):1415-1417
[53] Dumelie N, Benhayoune H, Richard D, Laurent-Maquin D, Balossier G. In vitro precipitation of electrodeposited calcium-deficient hydroxyapatite coatings on Ti6Al4V substrate. Mater Charact 2008; 59 : 129-133.
[54] Daltin A-L, Aahmed Chekkat A, Millet P, Chopart J-P. Electrocrystallization kinetics of hydroxyapatite and calcium phosphate coatings under magnetic fiel, Magnetohydrodynamics 2012;48(2):43-52
[55] LeGeros JP, Lin S, Mijares D, Dimaano F, LeGeros RZ. Electrochemically deposited calcium phosphate coating on titanium alloy substrates. Key Eng Mater 2005;284-286:247-250.
[56] Blackwood DJ, Seah KHW. Galvanostatic pulse deposition of hydroxyapatite for adhesion to titanium for biomedical purposes. Mater Sci Eng C 2010;30:561–565.
[57] Sadat-Shojai M, Khorasani MT, Jamshidi A, Hydrothermal processing of hydroxyapatite

nanoparticles - A Taguchi experimental design approach. J Cryst Growth 2012;361:73-84.
[58] Lukić MJ, Veselinović LJ, Stojanović Z, Maček-Kržmanc M, Bračko I, Škapin SD, Marković S et al. Peculiarities in sintering behavior of Ca-deficient hydroxyapatite nanopowders. Mater Lett 2012; 68:331-335.
[59] Mir M, Siddiqi SA, Hussain T, Chaudhry AA, Rehman IU, Khan AS, Abbas G. Synthesis and characterization of calcium deficient apatite granules for drug eluting bone graft applications. Ceramics Int 2014;40:10719-10725
[60] Leng Y, Chen J, Qu S. TEM study of calcium phosphate precipitation on HA/TCP ceramics, Biomaterials 2003;24:2125-2131.
[61] Dumelie N, Benhayoune H, Rousse-Bertrand C, Bouthors S, Perchet A, Wortham L, Douglade J et al. characterization of electrodeposited calcium phosphate coatings by complementary scanning electron microscopy and scanning trans-mission electron microscopy associated to X-ray microanalysis. Thin Solid Films 2005;492:131-139.
[62] Redepening J, Schlessinger T, Burnham S, Lippiello L, Miyano J. Characterization of electrolytically prepared brushite and hydroxyapatite coatings on orthopedic alloys. J Biomed Mater Res 1996;30:287-294
[63] Zhang H, Zhang M. Characterization and thermal behavior of calcium deficient hydroxyapatite whiskers with various Ca/P ratios. Mater Chem Phys 2011;126(3):64-648
[64] Raynaud S, Champion E, Bernache-Assollant D. Calcium phosphate apatites with variable Ca/P atomic ratio II. Calcination and sintering. Biomaterials 2002;23:1073-1080
[65] Han HM, Phillips GJ, Mikhalovsky SV, FitzGerald S, Lloyd AW. Sonoelectrochemical deposition of calcium phosphates on carbon materials : effect of current density. J Mater Sci: Mater Med 2008;19:1787-1791
[66] Gopi D, Karthika A, Sekar M, Kavitha L, Pramod R., Dwivedi J. Development of lotus-like hydroxyapatite coating on HELCDEB treated titanium by pulsed electrodeposition. Mater Lett 2013;105:216-219
[67] Zhang F, Wong SS, Ambient large-scale template-mediated synthesis of high-aspect ratio single-crystalline, chemically doped rare-earth phosphate nanowires for bioimaging. ACS Nano 2010;4(1):99-112.
[68] Hulteen JC, Martin CR. A general template-based method for the preparation of nanomaterials. J Mater Chem 1997;7(7):1075–1087.
[69] Keating CD, Natan MJ, striped metal nanowires as building blocks and optical tags, Adv Mater 2003;15(5):451-454.
[70] Ferraz MP, Monteiro FJ, Manuel CM. Hydroxyapatite nanoparticles : A review of preparation methodologies. J Appl Biomater Biomech 2004;2:74-80
[71] Xia Y, Yang P, Sun Y, Wu Y, Mayers B, Gates B, Yin Y et al. One-dimensional nanostructures : synthesis , characterization, and applications. Adv Mater 2003;15(5):353-389

[72] Wang H, Eliaz N, Hobbs LH. The nanostructure of an electrochemically deposited hydroxyapatite coating. Mater Lett 2011;65:2455-2457
[73] Thirsk HR, Harrison JR. A guide to the study of electrode kinetics. London ; New York : Academic Press; 1972, p118.
[74] Ertan A, Tewari SN, Talu O. Electrodeposition of nickel nanowires and nanotubes using various templates. J Exp Nanosci. 2008;3(4):287-295.
[75] Yoo WC, Lee JK. Field Dependent Growth Patterns of Metals Electroplated in Nanoporous Alumina Membranes Adv Mater 2004;16:1097.
[76] Martin RC. Nanomaterials: a membrane -based synthetic approach. Science, 266: 1994 : 1961-1966.
[77] Li X, Wang Y, Song G, Peng Z, Yu Y, She X, Li J. Synthesis and growth mechanism of Ni nanotubes and nanowires. Nanoscale Res. Lett. 2009;4 (9): 1015–1020.
[78] Liu L, Ma D., Blackley RA, Zhou W, Han X and Bao X. Synthesis and characterization of Gibbsite nanostructures, J. Phys. Chem. C. 2008:4124–4128.
[79] Spain E, McCooey A, Joyce K, Keyes TE, Forster RJ. Gold nanowires and nanotubes for high sensitivity detection of pathogen DNA. Sensors Actuators, B Chem. 2015;215:159-165.
[80] Cao H, Wang L, Qiu Y, Wang G, Zhang L, and Liu X, Generation and growth mechanism of metal (Fe, Co, Ni) nanotube arrays, Chemphyschem. 2006;7:1500–1504.
[81] Tourillon G, Pontonnier L, Levy JP, Langlais V. ChemInform Abstract: Electrochemically Synthesized Co and Fe Nanowires and Nanotubes. Electrochemical and Solid-State Letters,2000;**3**:20-23.
[82] Martin CR. Template synthesis of electronically conductive polymer nanostructures. Acc Chem Res, 1995, 28: 61-68.

Acknowledgments

The authors have a thought for Mr Patrick Baudart† for the preparation of electrochemical cell and little materials used. The authors thank Eric Gautron from the Institut des Matériaux Jean Rouxel IMN (Nantes, France) for his help to the TEM experiments and for access to the TEM facilities of IMN. This work was supported by the Fondation pour la Recherche Médicale, grant number DCM 20111223750 to Chopart.

Figures legend :

Fig. 1: CaP electrodeposition; a) experimental setup in a three electrodes electrochemical cell; b) two examples of potential versus time curves during electrodeposition in constant and pulsed mode; c) steps of CaP deposition in thin films and into track-etched and gold covered polycarbonate membranes followed by the collection of the nanowires after membrane dissolution in dichloromethane at 40°C. (for color reproduction in print)

Fig. 2: Cathodic part of cyclic voltammogram for thin films at a scan rate of 10 mV/s and 70°C.

Fig. 3: XRD patterns and Ca/P ratios of CaP thin films deposited on gold at various electrochemical conditions; (for color reproduction in print).

3': a, b, c, d: constant potentiostatic mode at -1.6 $V/_{Ag/AgCl}$;

3": e, f, g, h: constant and pulsed potential of -1.6V $/_{Ag/AgCl}$.

3"': XRD patterns of powders (obtained by milling thin films) respectively before and after heat treatment (HT; 850°C-2h) at -1.6V $/_{vs\ AgAgCl}$ potential, pulsed mode, 70°C for effective 15 min.

Fig. 4: 4' : SEM micrograph of the cross-section of a membrane with 200 nm pores diameter; **4" :** optic micrographs (after 5 minutes effective time of electrodeposition) of deposition on membranes: **a:** membrane seen on the deposition side; **b:** membrane seen on its lateral side; **c:** membrane seen on the deposition side with a grill interposed between cathode and membrane, d : membrane c seen on its lateral side. (for color reproduction in print)

Fig. 5: SEM micrographs : **a)** porous gold covering on a membrane with 100 nm nanopores diameter and 300 nm gold thickness; **b)** cross sectional view of gold coated polycarbonate membrane with 200 nm nanopores diameter; **c)** porous nanotubes obtained from 400 nm pores diameter membrane in pulsed mode (15 min effective deposition time, deposition time 1 s, break time 2 s); **d)** nanotubes seen from one tip, in membranes with 100 nm nanopores diameter; obtained in pulsed mode (15 min effective deposition time, deposition time 1 s, break time 2 s) **e)** nanotubes and nanowires synthesized from deposition in constant mode during 30 minutes at -1,6V /AgAgCl in membranes with 100 nm nanopores diameter; **f)** porous nanowires obtained from 100 nm pores diameter membranes in pulsed mode (15 min effective deposition time, deposition time 1 s, break time 2 s).

Fig. 6: TEM micrographs (bright field images **a, b**) of CaP nanowires for samples deposited in membranes with 200 nm pores diameter at pulsed potential of -1.6V $/_{Ag/AgCl}$ after 5 minutes effective deposition time; **V3-60k** (view a magnified), **V3-400k** (view V3-60k magnified); **d3 and d4**: selected area diffraction patterns taken in the nanowires (view a and b).

Fig. 7: TEM micrographs (bright field images **a, b**) of CaP nanowires for samples deposited in membranes with 200 nm pores diameter at pulsed current density of -120 mA/cm^2 after

5 minutes effective deposition time; **V1-500k and V1-400k** (view a magnified), **V2'-500k** (view b magnified); **d1'' and d2**: selected area electron diffraction patterns taken in the nanowires (view a and b respectively); **FT**: Fourier Transform from the squared area in V1-400k image and **$SEDP_{HA}$**: simulated electron diffraction pattern along the [010] zone axis of the HA unit cell.

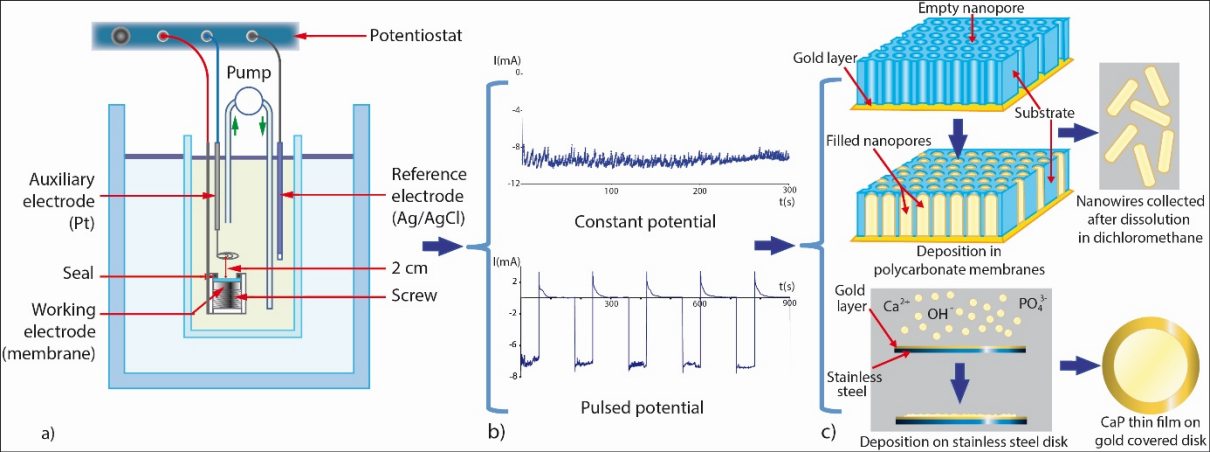
Fig. 8: TEM micrographs (bright field images **a, b**) of CaP nanotubes for samples deposited in membranes with 400 nm pores diameter at pulsed potential of -1.6V /$_{Ag/AgCl}$ after 5 minutes effective deposition time; **V3-400k'** (view b magnified); **d3''** : selected area diffraction patterns taken in the nanotubes (view a).

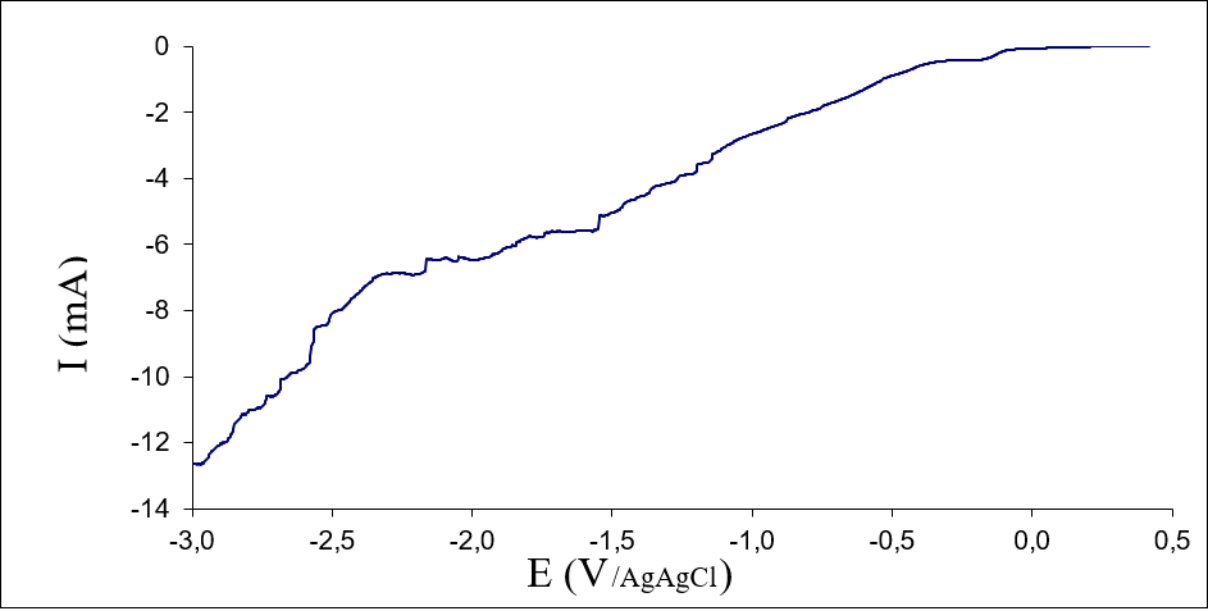
Fig. 9: Hypothesized schematic mechanism of nanotubes (**a and a'**) and nanowires (**b and b'**) growth : **a and b**) (longitudinal) cross sectional view of nanopores; **a' and b'**) deposited nanopore wall. (for color reproduction in print)

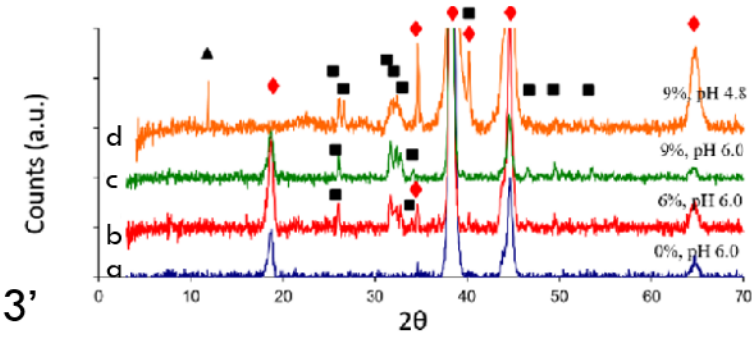
Table legend:

Table 1 : The electrochemical conditions of the CaP thin films samples varying by the % volume H_2O_2, pH of the electrolytic bath and electrical mode (constant or pulsed) at imposed potential value of -1.6 V/AgAgCl (g and c are two different samples obtained in the same conditions).

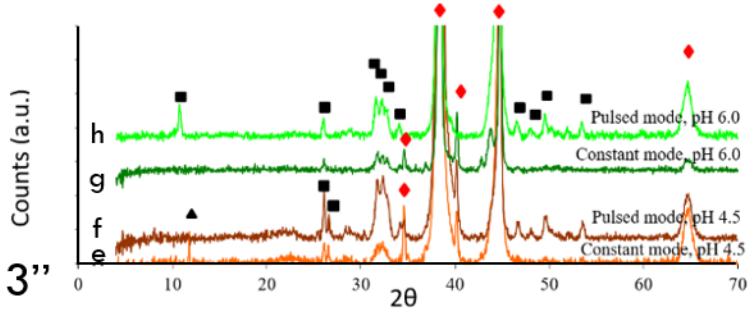
Table 2 : SEM micrographs of non-deposited membranes of 100, 200 and 400 nm pore diameters and CaP nanowires / nanotubes at 2 magnifications obtained from these membranes and their aspect ratios for samples deposited at pulsed potential in potentiostatic mode (t_{ON} = 1min at E=-1.6 / Ag/AgCl, t_{OFF} = 2 min at E= free potential) with varied durations of effective deposition (3, 5, 10 and 15 minutes) ; L = length, D = diameter.


Potentiostat
Pump
Auxiliary electrode (Pt)
Reference electrode (Ag/AgCl)
Seal
2 cm
Screw
Working electrode (membrane)
a)
I(mA)
0
-4
-8
-12
100
200
300
t(s)
Constant potential
I(mA)
2
-2
-6
-8
300
600
900
t(s)
Pulsed potential
b)
Empty nanopore
Gold layer
Substrate
Filled nanopores
Deposition in polycarbonate membranes
Nanowires collected after dissolution in dichloromethane
Gold layer
Ca^{2+}
OH^-
PO_4^{3-}
Stainless steel
Deposition on stainless steel disk
CaP thin film on gold covered disk
c)


0
-2
-4
-6
-8
-10
-12
-14
I (mA)
-3,0
-2,5
-2,0
-1,5
-1,0
-0,5
0,0
0,5
E (V/AgAgCl)



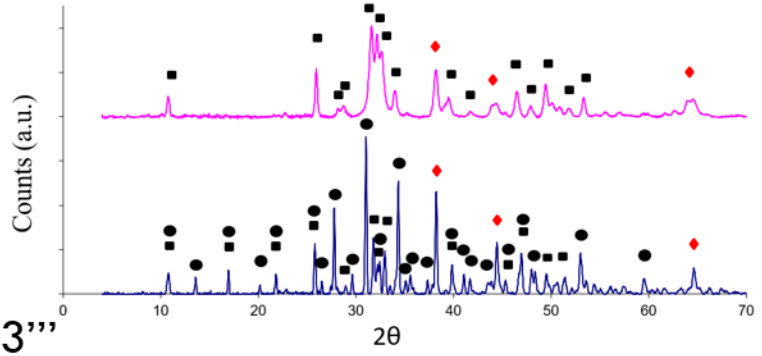
3’



3’’

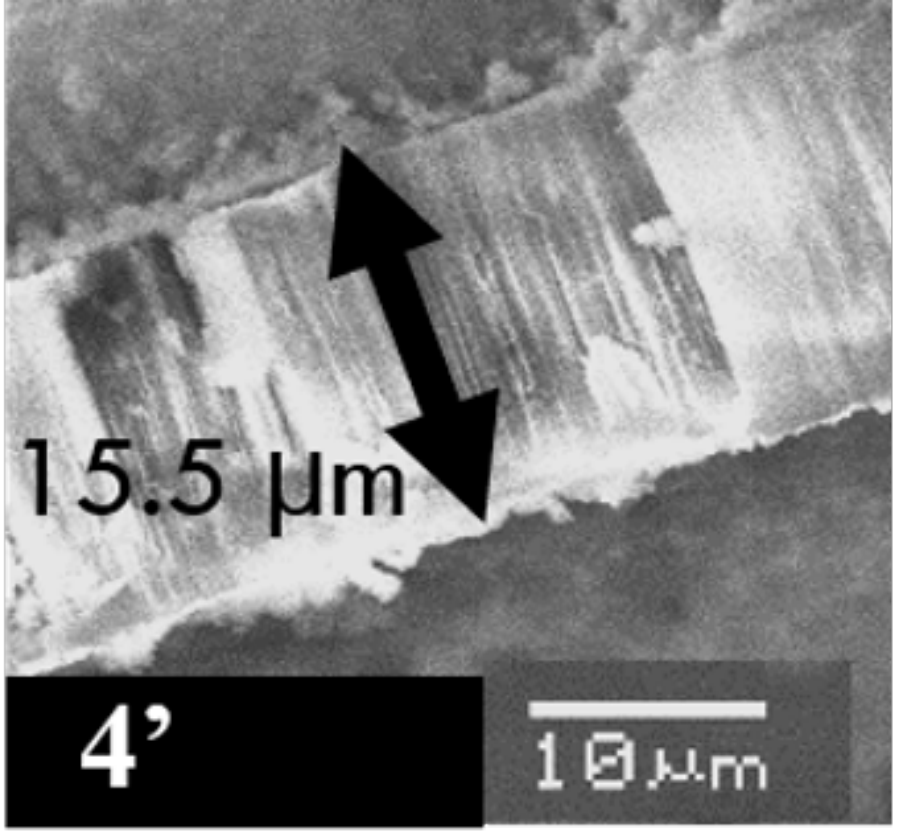
■ HA / OCP
▲ DCPD
◆ Substrate

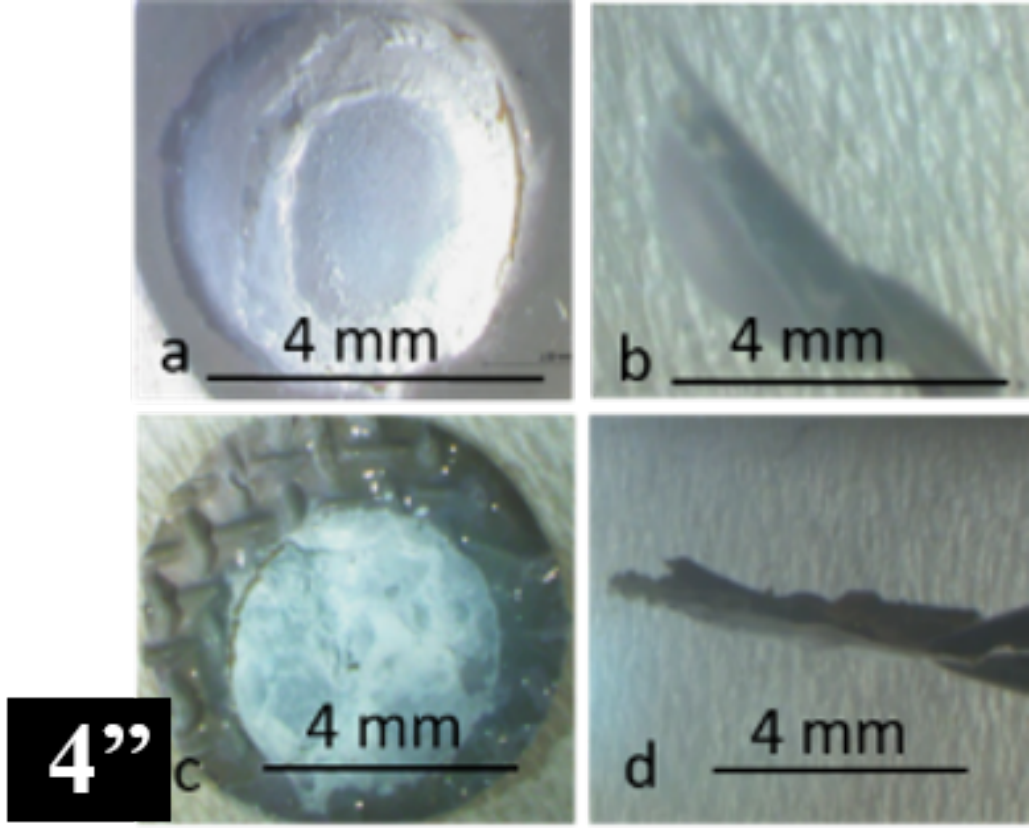
Samples	Ca/P ratios
a	/
b	1.53
c	1.57
d	1.46
e	1.46
f	1.52
g	1.74
h	1.55

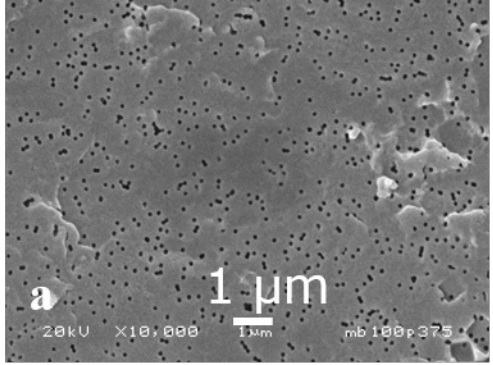


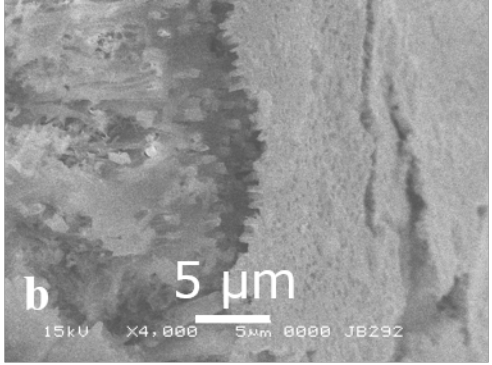
3’’’

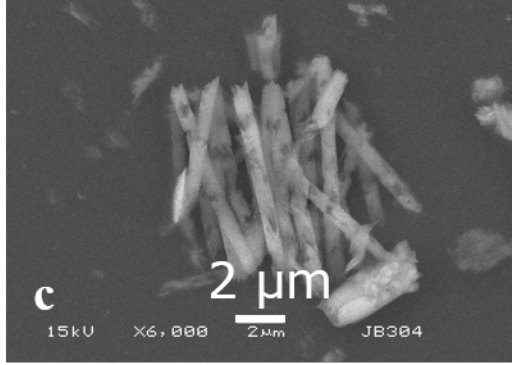
■ HA / CDHA
● β-TCP
◆ Substrate

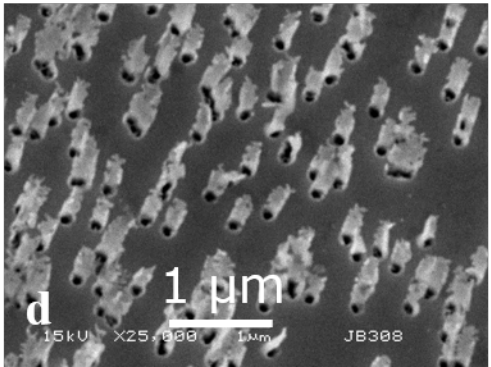

15.5 µm
4’
10 µm

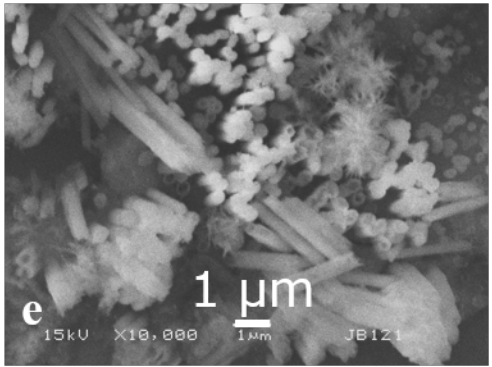

a
4 mm
b
4 mm
4”
c
4 mm
d
4 mm

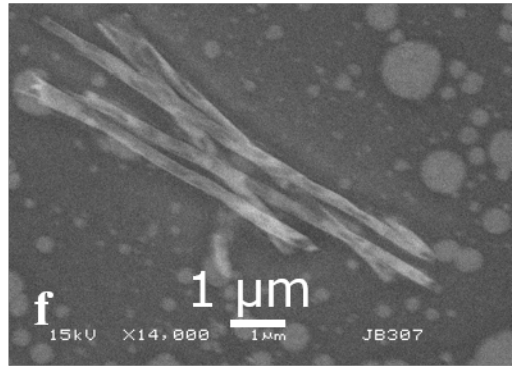

a
1 µm
20kV X10,000 1µm mb100p375

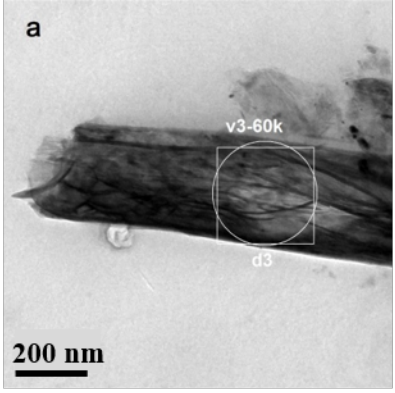

b
5 µm
15kV X4,000 5µm 0000 JB292

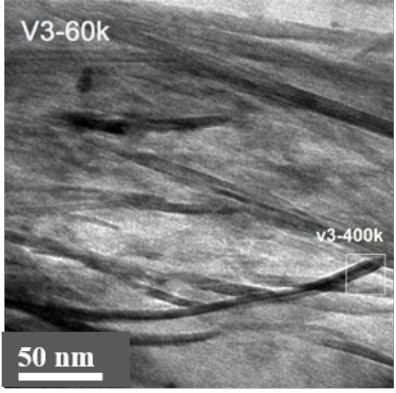

c
2 µm
15kV X6,000 2µm JB304

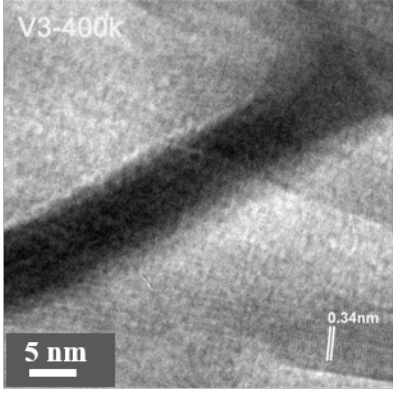

d
1 µm
15kV X25,000 1µm JB308

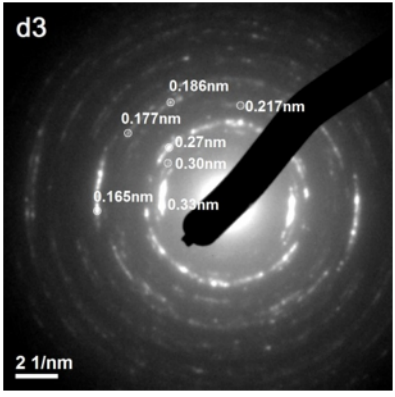

e
1 µm
15kV X10,000 1µm JB121

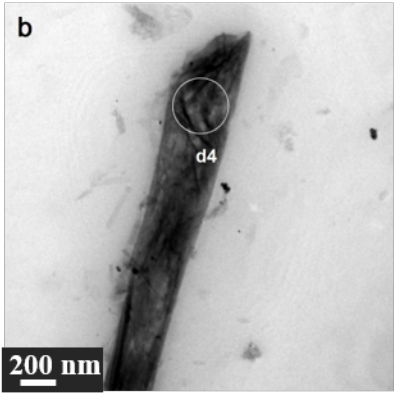

f
1 µm
15kV X14,000 1µm JB307

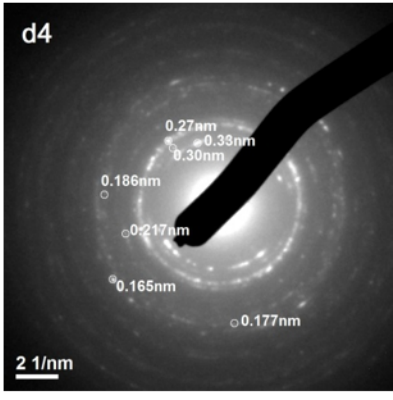

a
v3-60k
d3
200 nm

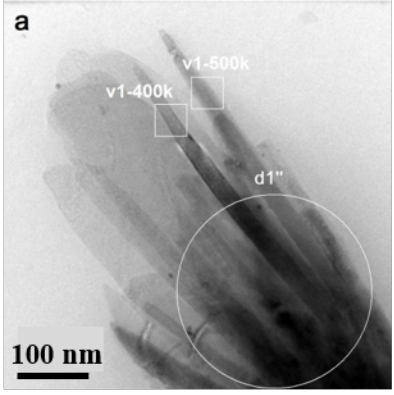

V3-60k
v3-400k
50 nm

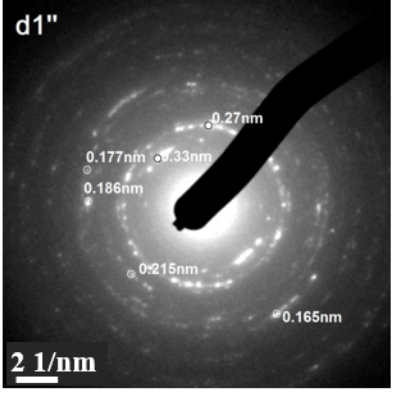

V3-400k
0.34nm
5 nm

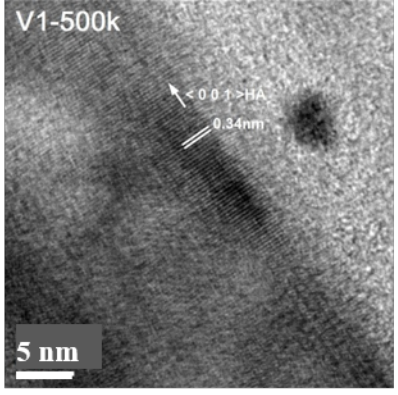

d3
0.186nm
0.217nm
0.177nm
0.27nm
0.30nm
0.165nm
0.33nm
2 1/nm

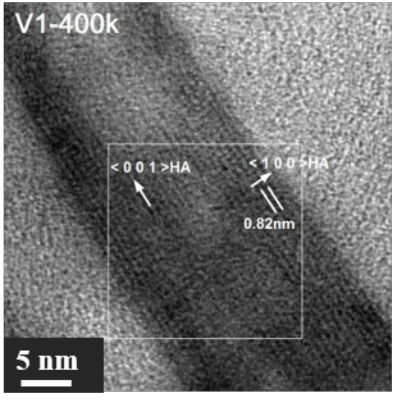

b
d4
200 nm

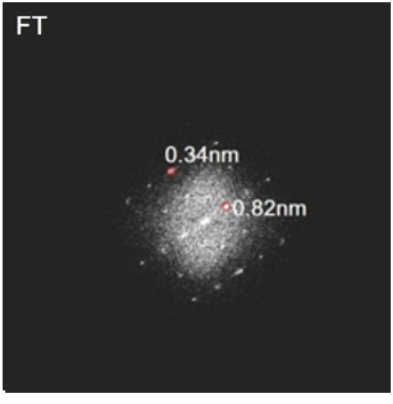

d4
0.27nm
0.33nm
0.30nm
0.186nm
0.217nm
0.165nm
0.177nm
2 1/nm

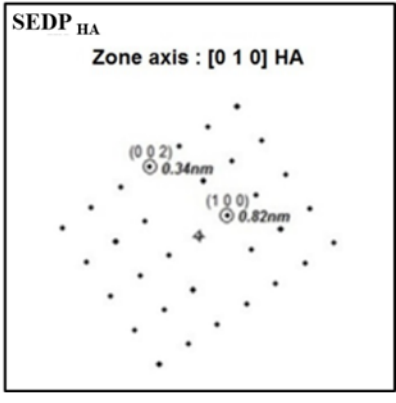

a
v1-500k
v1-400k
d1"
100 nm

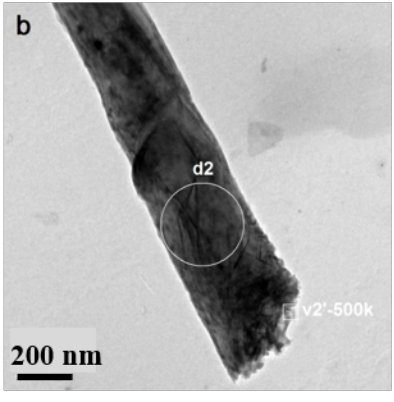

d1"
0.27nm
0.177nm
0.33nm
0.186nm
0.215nm
0.165nm
2 1/nm

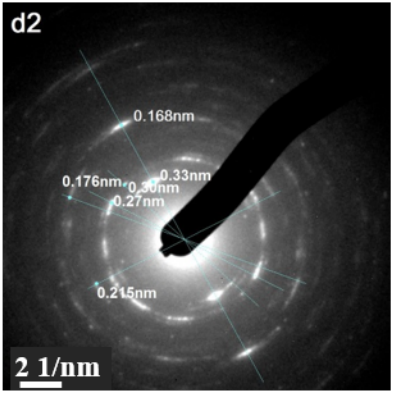

V1-500k
< 0 0 1 >HA
0.34nm
5 nm

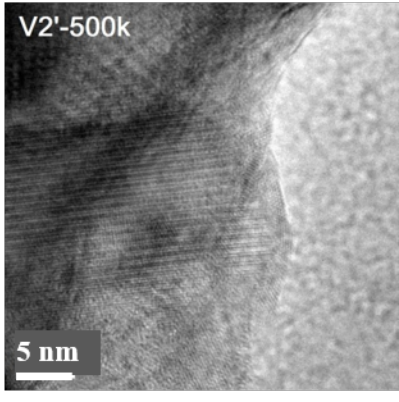

V1-400k
< 0 0 1 >HA
< 1 0 0 >HA
0.82nm
5 nm

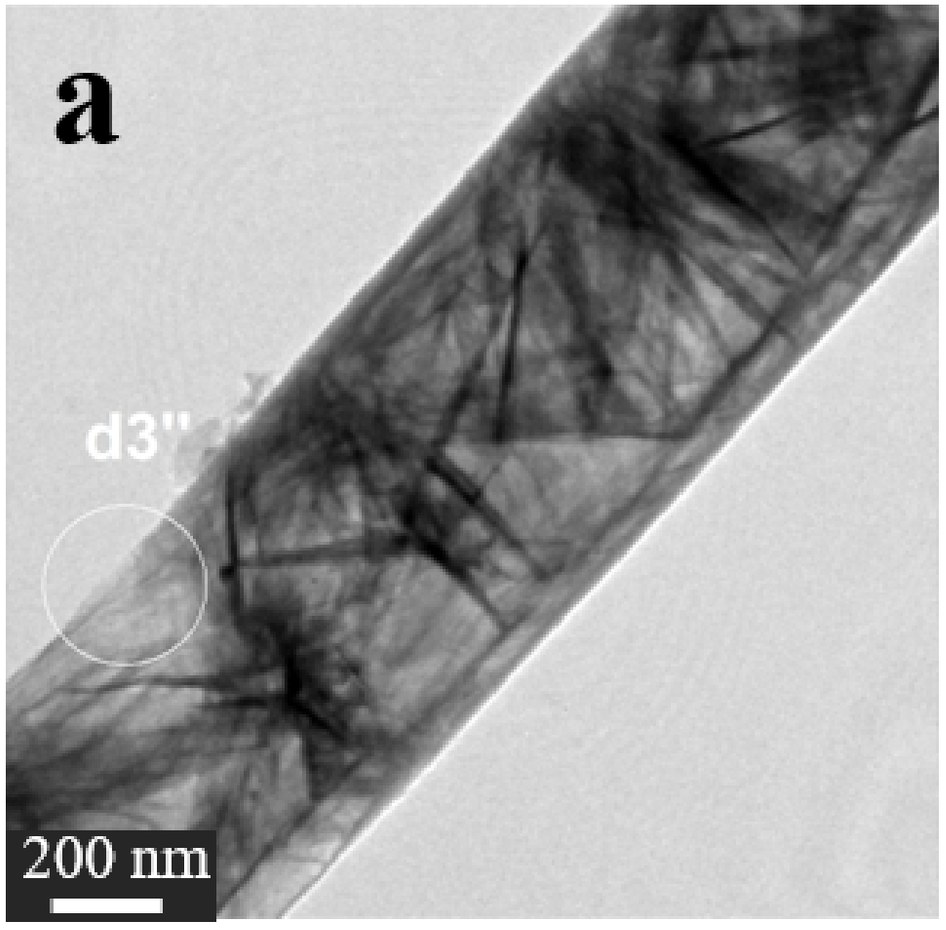

FT
0.34nm
0.82nm

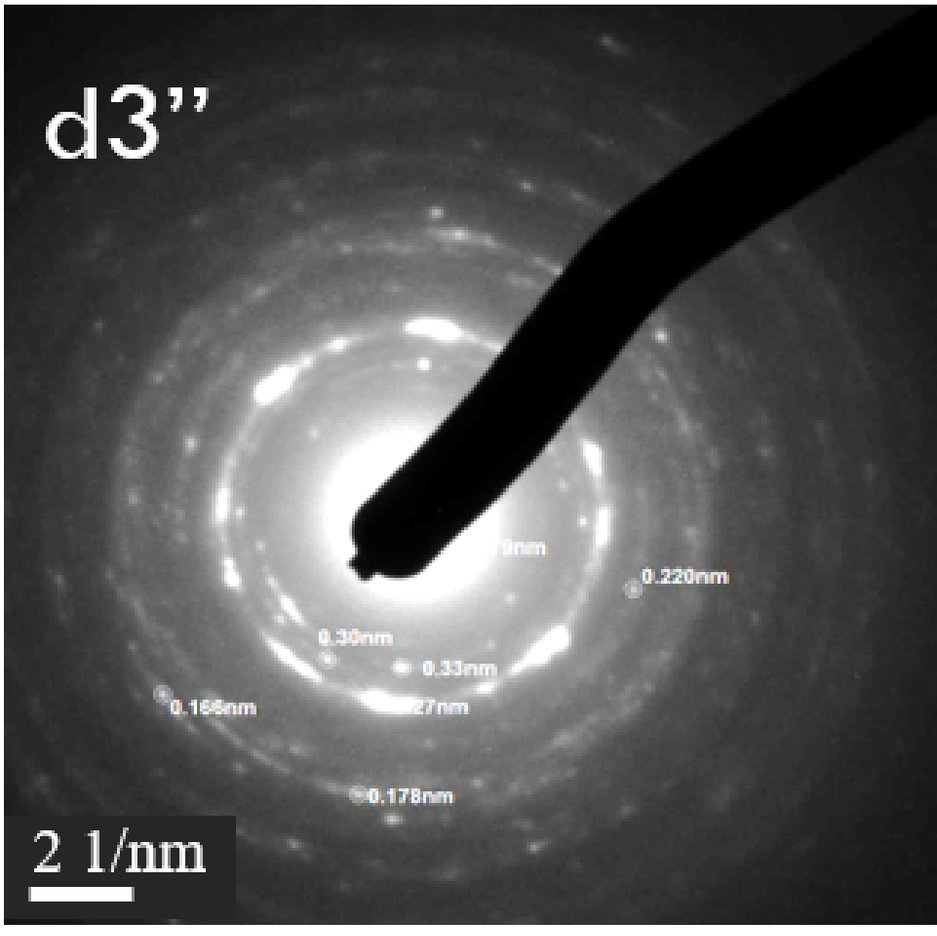

SEDP HA
Zone axis : [0 1 0] HA
(0 0 2)
0.34nm
(1 0 0)
0.82nm

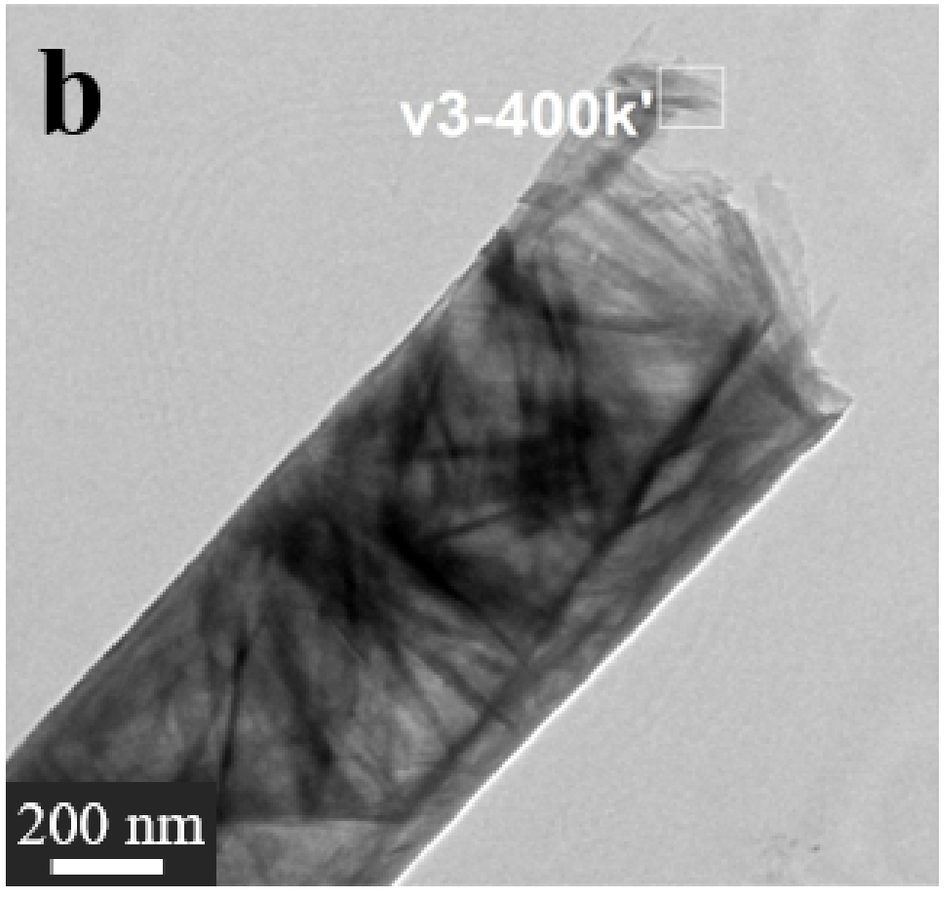

b
d2
v2'-500k
200 nm

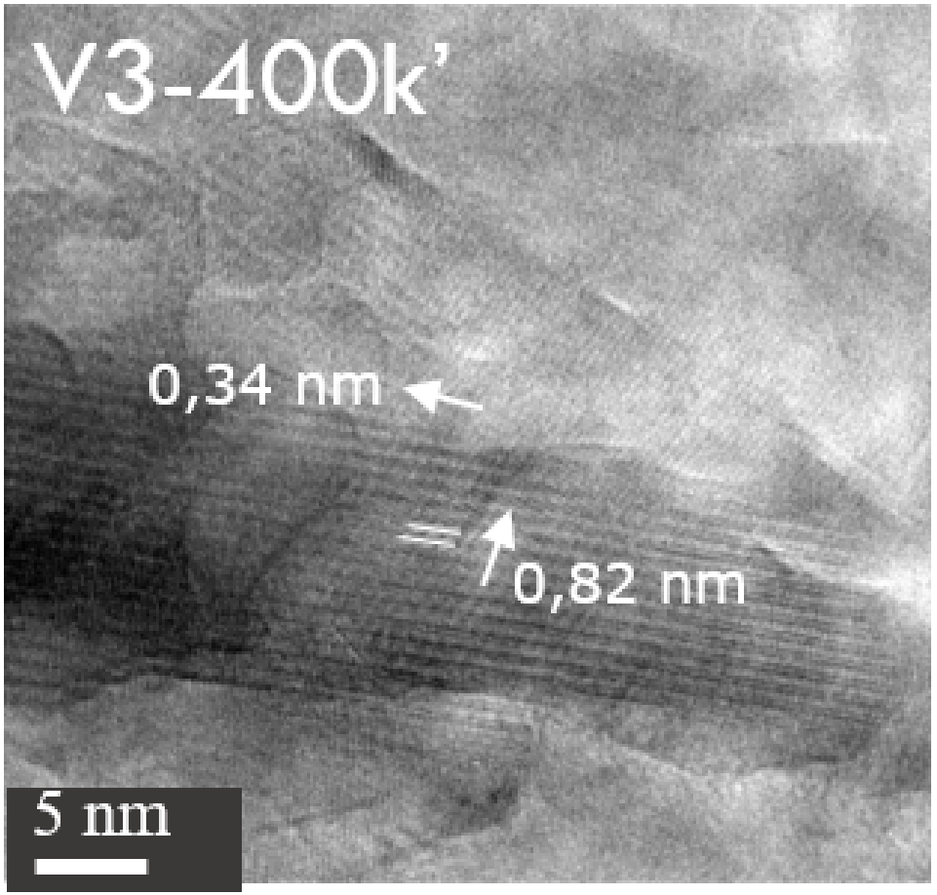

d2
0.168nm
0.176nm
0.33nm
0.30nm
0.27nm
0.215nm
2 1/nm

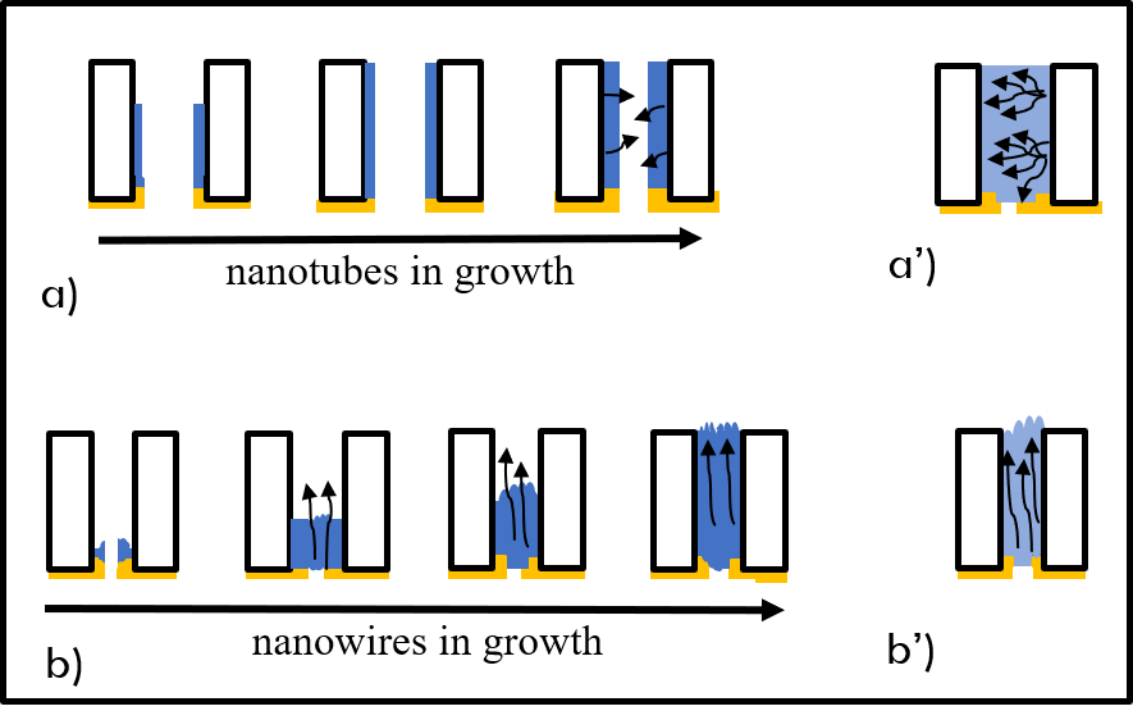

V2'-500k
5 nm


a
d3''
200 nm

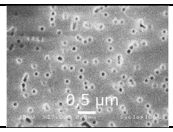
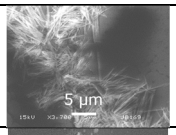
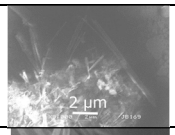
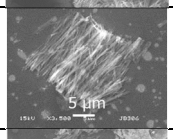
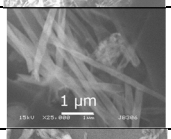
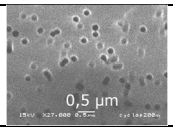
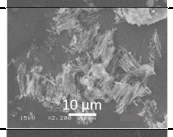
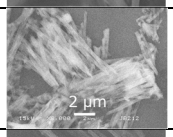
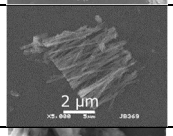
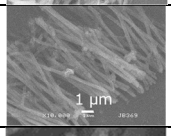
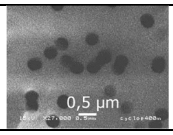
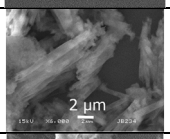
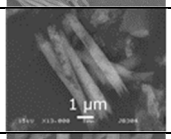
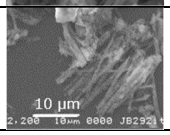
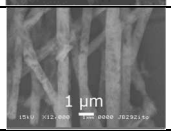

d3''
0.220nm
0.30nm
0.33nm
0.168nm
0.178nm
2 1/nm


b
v3-400k'
200 nm


V3-400k'
0,34 nm
0,82 nm
5 nm


nanotubes in growth
a)
a')
nanowires in growth
b)
b')

Samples	% vol H_2O_2	pH	Corresponding current density (mA/cm^2)	Electrical mode (constant or pulsed)
a	0	6.0	-1 / -50	constant
b	6	6.0	-120 / -160	constant
c	9	6.0	-80 / -110	constant
d	9	4.8	-50 / -75	constant
e	9	4.5	-55 / -75	constant
f	9	4.5	-80 / -40	pulsed
g	9	6.0	-80 / -115	constant
h	9	6.0	-65 / -90	pulsed

Membrane' pores diameters	Correspon-ding current density (mA/cm²)	Effective depositio n duration (min)	SEM micrographs of non-deposited membrane	SEM micrographs	SEM micrographs	Aspect ratios
100 nm	-120	3				20 - 43 (L 6.2 - 9.5 µm) (D 220 - 303 nm)
100 nm	-300	5				37 - 71 (L 12.9 - 15.9 µm) (D 222 - 350 nm)
200 nm	-220	5				19 - 22 L 7.2 - 8.3 µm) D 370 nm)
200 nm	-300	15				21 - 53 (L 5.7 - 14.5 µm) (D 270 nm)
400 nm	-270	5				10 - 19 (L 8.7 - 13.2 µm) (D 590 - 930 nm)
400 nm	-250	10				9 - 25 (L 8.6 - 15.6 µm) (D 620 - 970 nm)